Sapienza
Università di Roma

Facoltà di Scienze Matematiche, Fisiche e Naturali

Corso di Laurea in Fisica

Search for exotic resonances in the decay $B^+ \to J/\psi\,\omega\,K^+$ in the LHCb experiment at CERN

Tesi di Laurea Magistrale

Candidato
Guido Andreassi
Matr. 1258855

Relatore
Dr.ssa Roberta Santacesaria

Correlatore
Dr. Antonio Augusto Alves Jr

Anno Accademico 2013/2014

Contents

Introduction

The expression *exotic resonances* indicates those states whose characteristics don't fit in the ordinary mesons nor baryons scheme.
In this thesis an analysis of the $J/\psi\ \omega$ invariant mass in the decay $B^+ \to (J/\psi \to \mu^+\mu^-)\ (\omega \to \pi^+\pi^-\pi^0)\ K^+$ is performed in order to search for such resonances, in particular the X(3872), previously observed in this final state by the BaBar experiment in 2010 at the Stanford Linear Accelerator Center [10].

The nature of this particle is still under study: different theoretical models were proposed. Thus, further experimental measurements are needed in order to improve the understanding of its characteristics.

The present analysis is performed on data collected by the LHCb experiment at the Large Hadron Collider at CERN during 2011 and 2012. It is structured as follows:

- the events are reconstructed and selected in order to reduce as much as possible the background contamination;
- the Monte Carlo dataset is analysed in order to study the characteristics of the signal events and the expected resolutions;
- a statistical background subtraction is performed and the $J/\psi\ \omega$ invariant mass is analysed;
- additional contributions from other decays are searched for and eliminated where possible;
- the efficiency of the selection chain is calculated from MC data and used to correct the $J/\psi\ \omega$ data distribution;
- the efficiency-corrected $J/\psi\ \omega$ mass spectrum is compared to BaBar's results;
- a double peak structure is observed in the low mass region of the $J/\psi\ \omega$ invariant mass spectrum, and it is attributed to the two charmonium states $\chi_{c0}(2P)$ and X(3872);

- the relative yields of the two contributions are evaluated and compared to those reported by BaBar;
- future perspectives are illustrated.

Chapter 1

The exotic states

The proliferation of discoveries of strongly interacting subatomic particles in the first half of the 20^{th} century led to the need of a theory allowing a classification and the explanation of the known states or even the prediction of new ones. [38, 42]

A first attempt, consisting in describing all the resonances as proton-neutron bound states, was made in 1949 by E. Fermi and C. N. Yang, and subsequently extended in 1959 by S. Sakata, who added to this (p, n) pair the isosinglet hyperon Λ, in order to include the *strange* particles.
However, this model met with serious difficulties in predicting baryons' masses, spins and parities. In terms of group theory, the Fermi-Yang model is described by the group SU(2), while the Sakata model is based on SU(3).
It is on the latter that, in 1961, M. Gell-Mann and Ne'eman based what they called the *eightfold way* model [49], in which mesons and baryons were grouped into multiplets of SU(3), namely octects for mesons and spin $\frac{1}{2}$ baryons and a decuplet for spin $\frac{3}{2}$ baryons (which correctly predicted the existence of the Ω^- baryon, discovered two years later at Brookhaven National Laboratory [4]).
Although very successful, this model didn't provide an explanation in terms of elementary constituents.

The search for such "fundamental bricks" led to the quark model, first postulated in 1964 by M. Gell-Mann [39] and, independently, George Zweig [58].
In the Gell-Mann Zweig scheme all the hadrons are composed of the three quarks u (up), d (down) and s (strange), and their respective anti-quarks: mesons are formed from quark and antiquark ($q\overline{q}$) pairs and baryons from three-quark triplets (qqq).
This model, later modified in order to include c (charm), t (top) and b (bottom) quarks, is currently known as the "Constituent Quark Model" (CQM) and still represents an

effective scheme for classifying all the known hadrons.
Among the generators of the SU(3) algebra, the so called Gell-Mann matrices, only two commute, and they are related to isospin I and hypercharge Y: these two quantities label each particle in each meson and baryon multiplet.

Using the Kronecker decomposition [36,54,56], Mesons and Baryons can be expressed as follows:

$$\begin{aligned} &\text{Mesons:} \quad && \mathbf{3} \otimes \overline{\mathbf{3}} = \mathbf{1} \oplus \mathbf{8} \\ &\text{Baryons:} \quad && \mathbf{3} \otimes \mathbf{3} \otimes \mathbf{3} = \mathbf{1} \oplus \mathbf{8} \oplus \mathbf{8} \oplus \mathbf{10} \end{aligned} \tag{1.0.1}$$

The current understanding is that the forces that bind quarks into hadrons are described by Quantum Chromodynamics (QCD), which is a non-abelian field theory.
To date, models that incorporate general features of the QCD theory are revealing to be extremely useful for describing properties and spectra of hadrons. A prediction of these QCD-motivated models, supported by lattice QCD[1], is the existence of hadrons with more complex substructures than the simple $q\overline{q}$ mesons and the qqq baryons, such as hybrids and multiquark states of either molecular or tetraquark configuration [37].
In the recent years, some (candidate) states whose characteristics don't fit in the ordinary mesons nor baryons have been indeed observed. Such particles are known as *exotic* states.

1.1 Exotic mesons

A tag can be assigned to a given particle using its total angular momentum $J = L \oplus S$, its parity P and its charge conjugation C, conventionally indicated as J^{PC}. The basic rules of quantum mechanics dictate that a $q\overline{q}$ meson can only have certain values of J^{PC}. However, as above mentioned, the theory does not, in principle, exclude the existence of more complex states which could have different combinations of quantum numbers, and some recent results from various experiments seem to strenghten this idea. [46]
In the light quark sector, for example, the $f_0(980)$ and the $a_0(980)$ are considered to be strong candidates for $K\overline{K}$ molecules. However, the high density of non-exotic light mesons due to the small mass difference between light quarks, makes it quite difficult to disentangle these states from the background.
A very thriving sector from this point of view is that of *charmonia* ($c\overline{c}$ states), which provides a cleaner environment. [40, 41]

[1] Lattice QCD is a numerical, discretized approach to calculate hadronic properties. See [53].

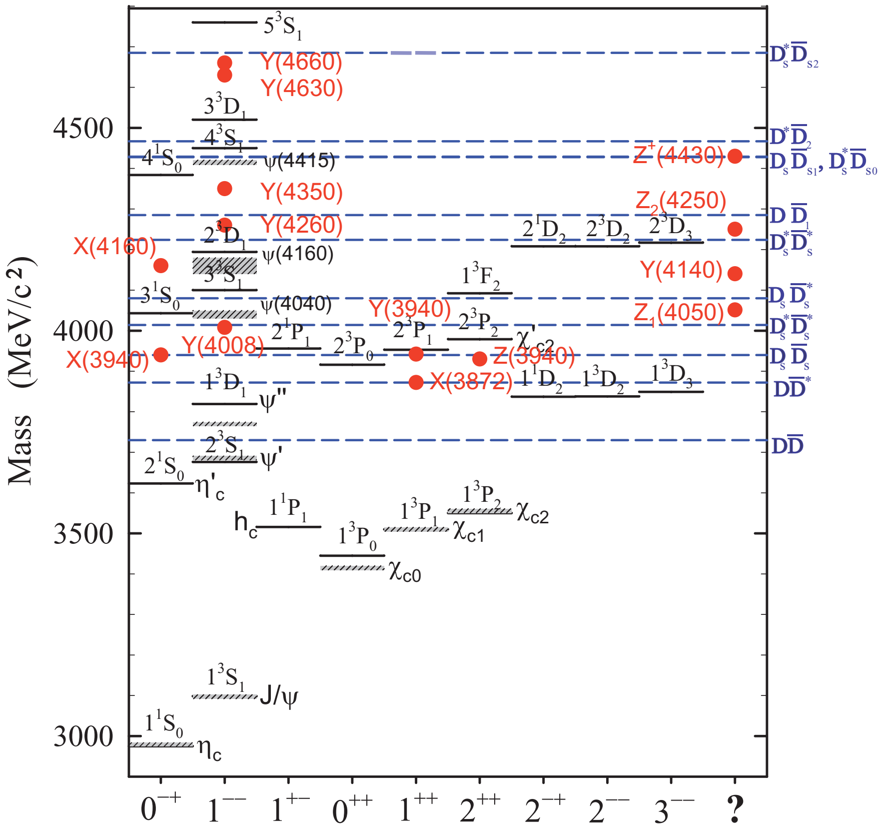

Figure 1.1: Charmonium spectrum.

1.1.1 Exotic charmonia

Figure 1.1 shows the spectrum of charmonium states where the solid segments represent the CQM predictions, the shaded segments are the observed conventional charmonium states, and the red dots are the exotic candidates placed in the most probable spin assignment column. Finally, the dashed lines show some $D\overline{D}$ production thresholds.

"Conventional" charmonium states are described by QCD as a $c\bar{c}$ couple, bounded by a short distance force dominated by a single gluon exchange, plus a linearly increasing confining potential. The energy levels are computed by solving a non-relativistic Schrödinger equation with this potential, while the splitting within multiplets is caused by a spin-dependent correction of order $(v/c)^2$.

This phenomenological description has revealed to be notably efficient in predicting and describing the observed charmonium states until the observation of a narrow peak in the $J/\psi\pi^+\pi^-$ invariant mass spectrum at 3872 MeV/c^2 by the Belle Collaboration 2003 [12]. This evidence led to the supposition of the existence of an exotic state, which has been named X(3872).

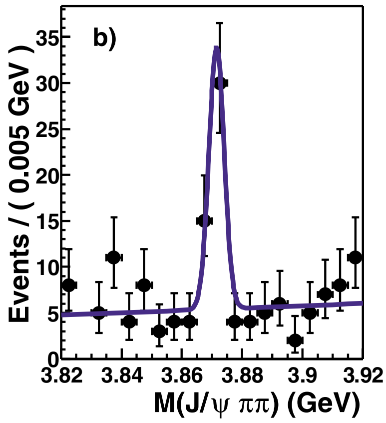

Figure 1.2: The peak in $J/\psi\pi^+\pi^-$ invariant mass observed by Belle.

Later observations of other neutral exotic states decaying into charmonium or $D^*\overline{D}$ pairs, made in different experiments have then enriched this scenario.
Three charged structures, named $Z^-(4430)$, $Z^-(4050)$ and $Z^-(4250)$ were also observed in 2008 by Belle [16,17], to which a fourth one, the $Z_c^+(3900)$ (observed in BESIII [35]) has recently added. The charge of these particles makes it even more evident that they can't be classified as $c\bar{c}$, and their minimal quark content must be $c\bar{c}d\bar{u}$.

1.2 The X(3872)

1.2.1 Experimental status

In 2003, an analysis of the decay $B \to K^+\pi^+\pi^- J/\psi$ from Belle revealed a narrow peaking structure in the invariant mass of $J/\psi\pi^+\pi^-$ (Figure 1.2).
In the following year, CDF [18] and D0 [21] observed an analogous peak and, in 2005, so did BaBar [8].
The invariant mass of $\pi\pi$ is consistent with the hypothesis of originating from $\rho \to \pi^+\pi^-$.
In addition to this, the decay $X(3872) \to J/\psi\gamma$ has been observed [9,13], indicating that the X(3872) has charge conjugation $C = +1$ and thus supporting the idea that the pions couple comes from a ρ meson. Further confirmations came from CDF [19].
This implies that the X(3872) cannot be an excited charmonium state, as that decay would violate isospin conservation.

Moreover, BaBar observed evidence for the decay $X(3872) \to J/\psi\omega$ at a rate comparable to that of $J/\psi\pi\pi$ [10], namely:

J^{PC}	decay	LS	χ^2 (11 d.o.f.)	χ^2 prob.
1^{++}	$J/\psi\rho^0$	01	13.2	0.28
2^{-+}	$J/\psi\rho^0$	11,12	13.6	0.26
1^{--}	$J/\psi(\pi\pi)_S$	01	35.1	2.4×10^{-4}
2^{+-}	$J/\psi(\pi\pi)_S$	11	38.9	5.5×10^{-5}
1^{+-}	$J/\psi(\pi\pi)_S$	11	39.8	3.8×10^{-5}
2^{--}	$J/\psi(\pi\pi)_S$	21	39.8	3.8×10^{-5}
3^{+-}	$J/\psi(\pi\pi)_S$	31	39.8	3.8×10^{-5}
3^{--}	$J/\psi(\pi\pi)_S$	21	41.0	2.4×10^{-5}
2^{++}	$J/\psi\rho^0$	02	43.0	1.1×10^{-5}
1^{-+}	$J/\psi\rho^0$	10,11,12	45.4	4.1×10^{-6}
0^{-+}	$J/\psi\rho^0$	11	104	3.5×10^{-17}
0^{+-}	$J/\psi(\pi\pi)_S$	11	129	$\leq1\times10^{-20}$
0^{++}	$J/\psi\rho^0$	00	163	$\leq1\times10^{-20}$

Table 1.1: Result of the $X(3872)$ particle angular analysis performed by CDF. Listed are the state, the decay mode, the L and S quantum numbers of the J/ψ-$(\pi^+\pi^-)$ system, the χ^2 with 11 degrees of freedom and the χ^2 probability.

$$\frac{BR(X(3872) \to J/\psi\omega)}{BR(X(3872) \to J/\psi\pi\pi)} = 0.8 \pm 0.3 \tag{1.2.1}$$

suggesting that X(3872) could be a mixture of isospin I=0 and I=1 states.

In 2007, CDF performed an angular analysis of the final state particles in the decay $X(3872) \to J/\psi\pi^+\pi^-$, where the $X(3872)$ is produced inclusively in the $p\overline{p}$ interaction [20]. The results, shown in Table 1.1, ruled out all the J^{PC} assignments except for 1^{++} and 2^{-+}.

The LHCb collaboration recently reported an analysis of the decay chain $B^+ \to X(3872)K^+ \to J/\psi\pi^+\pi^-K^+$, with $J/\psi \to \mu^+\mu^-$, rejecting the 2^{-+} hypothesis with an 8.2σ significance [34].

On the contrary, BaBar's analysis of the decay $X(3872) \to J/\psi\omega$ seemed to favour the 2^{-+} hypothesis with a confidence level of CL = 68%, without, however, being able to exclude the 1^{++} hypothesis (C.L. 7%). The results of both BaBar's and LHCb's analysis are shown in Figure 1.3 and 1.4.

This experimental scenario, therefore, rules out the explanation of the X(3872) meson as the conventional 2^{-+} $c\bar{c}$ state η_{c2} (1^1D^2 state predicted by QCD, close in mass to the

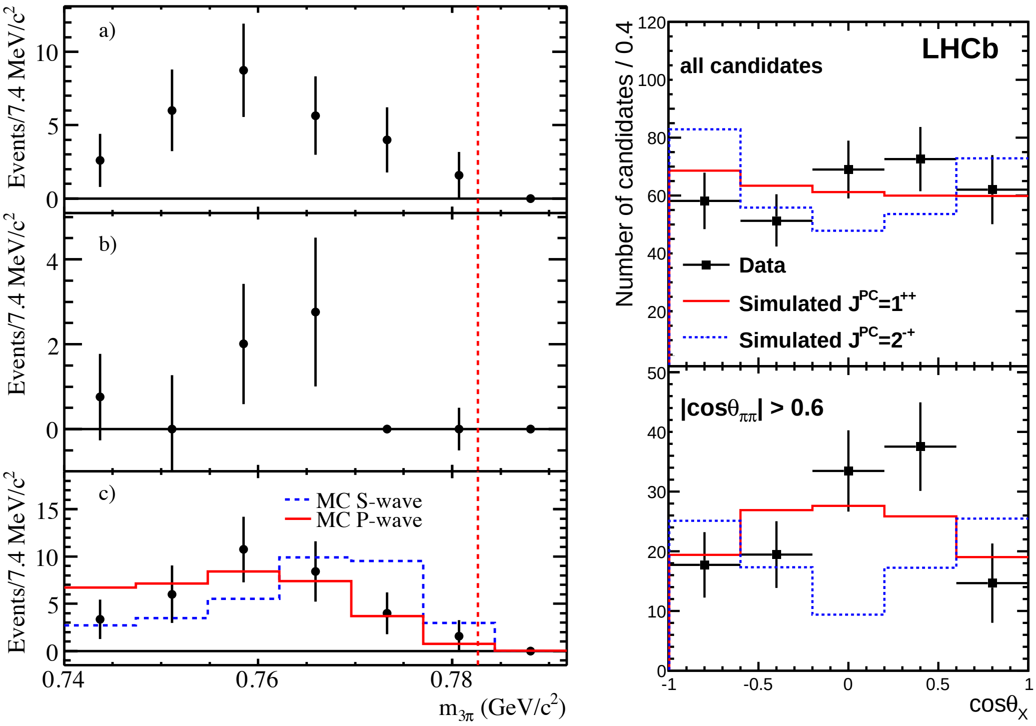

(a) BaBar: 3π mass distribution (b) LHCb: helicity angle distribution.

Figure 1.3: Determination of X(3872) quantum numbers: Figure 1.3(a) shows the $\pi^+\pi^-\pi^0$ mass distribution analysis from BaBar, while Figure 1.3(b) shows LHCb's helicity angle distribution analysis.

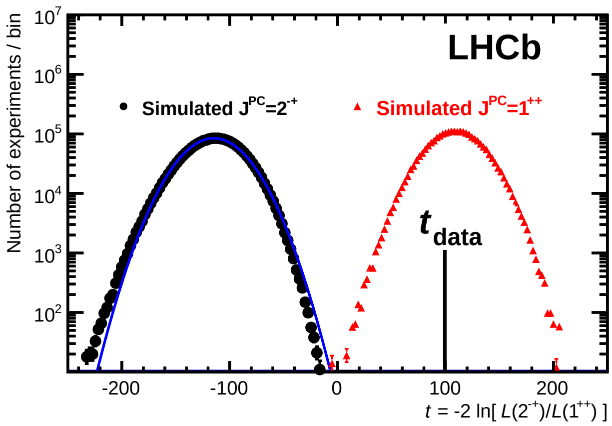

Figure 1.4: Distribution of the test statistics t for the simulated experiments with 2^{-+} and 1^{++} at LHCb.

X(3872), shown in Figure 1.1).
The remaining interpretations are discussed hereinafter.

1.2.2 Theoretical models

The $c\bar{c}$ state with $J^{PC} = 1^{++}$ is the χ'_{c1} (2^3P_1), with a mass predicted to be $3908 MeV/c^2$. This charmonium, predicted by the theory, has not been observed yet. However, as above mentioned, this hypothesis would imply the non-conservation of isospin [19].
Therefore, the unexpected features of the X(3872) probably need to be explained with some "alternative" theoretical model. Among the many ideas which have been proposed [41], at the present moment the most plausible are:

- **Mesonic molecule** [3, 7]: the fact that X(3872)'s mass is very close to the sum of a D^0 and a D^{*0} mesons led to the speculation that it could be a bound state of these two mesons with the tiny binding energy of $\epsilon_0 \simeq 0.25\ MeV/c^2$. This means that this molecule would have a very large radius ($R \simeq (2M_D\epsilon_0)^{-\frac{1}{2}} = 8fm$), which would allow the molecule to decay autonomously. The isospin violation would be explained by the fact that this molecule's wavefunction is expected to contain an admixture of $J/\psi\rho$ and $J/\psi\omega$.
  This small binding energy would, however, imply a small allowed range of relative center of mass momentum of the two mesons to form a molecule in hadronic colliders. A simulation performed in 2009 [5] shows the integrated prompt production cross section as a function of the relative momentum (see Figure 1.5). This allows to estimate the theoretical prompt production cross section of X(3872) at CDF under the mesonic molecule hypothesis.
  This cross section has been found to be approximately 0.085 nb in the phase space region that would allow the formation of the open charm meson pair constituting the molecule. This value is about 40 times smaller than the lower bound on the CDF experimental cross section (3.1 nb) [20].

- **Tetraquark** [45]: this model considers four-quark states of the form $[cq][\overline{cq}]$, where, in this case q can only be u or d, due to the X(3872) mass, giving thus the two possible neutral flavour states $X_u = [cu][\overline{cu}]$ and $X_d = [cd][\overline{cd}]$. The mass eigenstates are obtained by mixing the flavour states through a rotation matrix of a mixing angle θ:
  $$\begin{bmatrix} X_{low} \\ X_{high} \end{bmatrix} = \begin{bmatrix} cos\theta & sin\theta \\ -sin\theta & cos\theta \end{bmatrix} \begin{bmatrix} X_u \\ X_d \end{bmatrix} \tag{1.2.2}$$
  and they have a mass difference of $\Delta M = (7 \pm 2)/cos(2\theta) MeV/c^2$. The mixing angle can be determined by the ratio of 3π to 2π decay rates and it's found to be

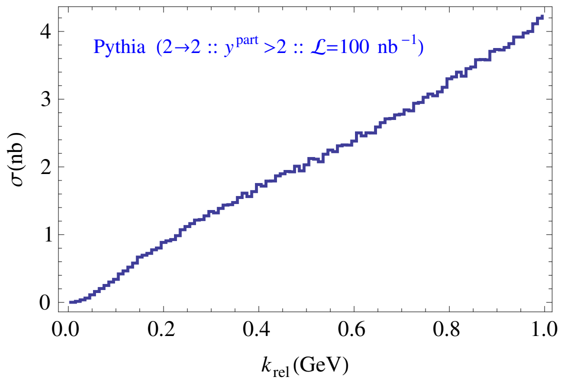

Figure 1.5: Simulation of the prompt production cross section as a function of the relative centre of mass momentum of the system $D^0\,\overline{D}^{*0}$ (k_{rel}).

about 20° from BaBar data.
This means that this model predicts a neutral exotic partner for the X(3872), with a mass difference of $8 \pm 3\ MeV/c^2$ along with other partners according to the spin-spin interactions between diquarks (which can be scalar or vector).
One of the two mass eigenstates defined in Equation 1.2.2 is predicted to be produced only in B^+ (or B^-) decays, while the other is expected exclusively from B^0 decays. This involves that the X(3872) seen in charged B decays and the one seen in neutral B decays are different states with mass difference ΔM.
However, the mass difference between the candidate X(3872) from these two sources was computed by Belle and resulted to be $\Delta M = 0.9 \pm 0.9\ MeV/c^2$, that is consistent with zero [15].
Figure 1.6 shows the spectrum of the X ($[cq][\overline{cq}]$) predicted by this theory. At the present moment, the X(3872) seems to be the only one of these predicted states to have been observed. The possibility of interpreting one of the predicted states with mass 3952 as another particle, the X(3940) observed by Belle [14], is also put forth in [45].

Other models that have been suggested (cusp close to $D^0\overline{D}^{*0}$ threshold, dynamically generated resonance, hybrid $c\bar{c}g$ resonance) seem not to fit properly with experimental data and are regarded as more unlikely with respect to the aforementioned ones.

1.2.3 The $J/\psi\ \omega$ decay channel

The observation of the decay X(3872) $\to J/\psi\ \omega$ was reported, as above mentioned, by BaBar in 2010 both in B^+ and B^0 decays to X(3872) K [10].
The number of observed signal events is 21.1 ± 7.0 for B^+ and 5.6 ± 3.0 for B^0, leading to a combined signal consisting of 34.0 ± 6.6 events. The probability of this enhancement

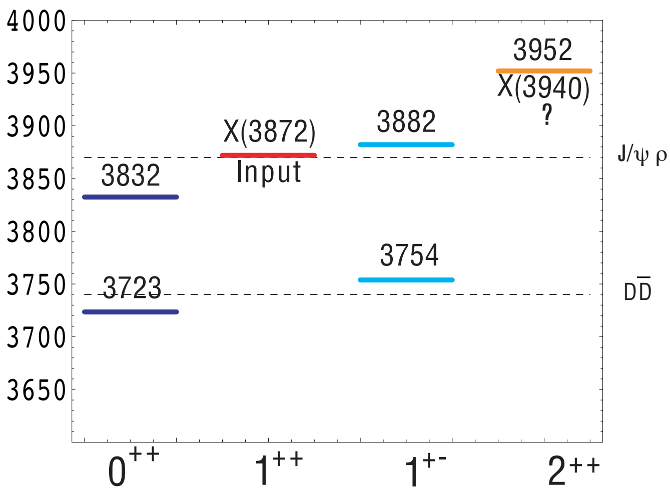

Figure 1.6: The full spectrum of the X particles predicted by the tetraquark model. The fine mass splitting described in Eq. 1.2.2 is not shown here.

being a background statistical fluctuation is 3.6×10^{-5}, corresponding to a significance of 4.0σ for a normal distribution.
Figure 1.7 shows the efficiency-corrected $J/\psi\ \omega$ invariant mass distribution for charged and neutral B decays, fitted with a function composed by a nonresonant background function and two gaussian peaks, corresponding to the X(3872) and a second peak at $\sim 3940\ MeV/c^2$. The latter, initially called Y(3940), has been a candidate exotic state until 2012 when the measurement of its quantum numbers performed by BaBar led to the identification with the excited charmonium state $\chi_{c0}(2P)$ [11].

Since $M(X(3872)) < M(J/\psi)+M(\omega)$, the decay $X(3872) \to J/\psi\ \omega$ is sub-threshold. This implies that only a low-mass ω contributes to this decay (since the J/ψ is extremely narrow).
BaBar measured a branching ratio for the charged B channel of:

$$BR(X(3872) \to J/\psi\omega) \times BR(B^+ \to X(3872)K^+) = (6 \pm 2 \pm 1) \times 10^{-6} \tag{1.2.3}$$

which, combined with the PDG value of

$$BR(B^+ \to X(3872)K^+) < 3.2 \times 10^{-4} \tag{1.2.4}$$

gives the limit:

$$BR(X(3872) \to J/\psi\ \omega) > 0.019 \tag{1.2.5}$$

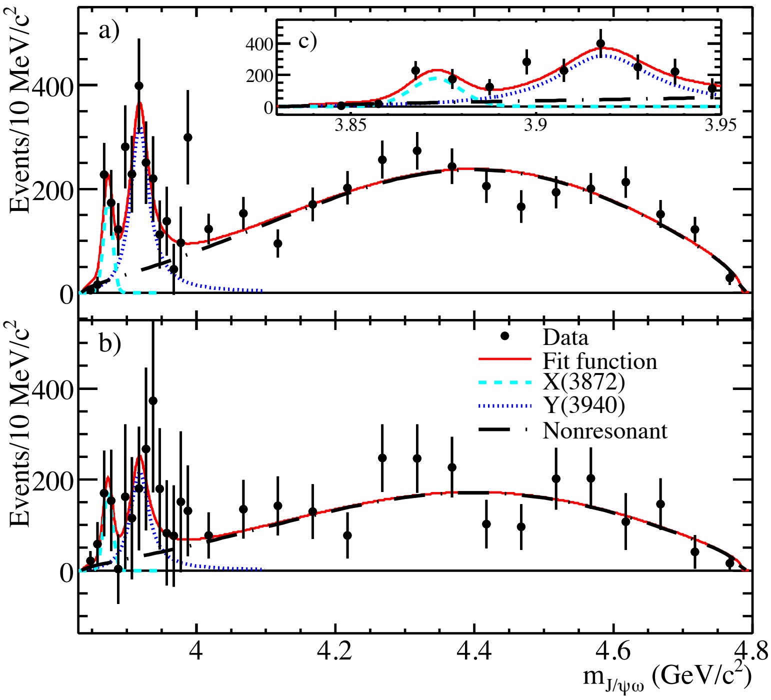

Figure 1.7: Corrected $M(J/\psi\omega)$ distribution for B^+ (top) and B^0 (bottom) decays as observed by BaBar in 2010.

The measurements of X(3872)'s quantum numbers have already been discussed under 1.2.1.

The final state $J/\psi\rho$ has isospin I=1, while $J/\psi\omega$ has I=0; as previously reported, both have been observed from X(3872) with similar branching ratios. This could mean that this particle is an admixture of states with different isospin, which in turn implies that those decaying into the two states are actually two different particles.

Repeating the angular analysis already performed on the $J/\psi\pi\pi$ channel for the $J/\psi\omega$ final state, would probably allow to understand whether we are dealing with one or two distinct particles.

The study of this channel is, for the reasons shown in this chapter, an interesting topic which could answer some of the still open questions and provide more precise measurements of its characteristics, such as the branching ratio and the quantum numbers.

Chapter 2

The LHCb experiment

The LHCb detector is specifically designed for precise measurements in the heavy flavour sector. Its primary goal is to search for evidence of new physics in CP violation and rare decays of hadrons containing beauty and charm quarks.
The present section contains a brief description of the experimental apparatus used to collect the data analysed in this thesis. After a quick general overview of the accelerator and the detector, the main sub-detectors and their performance are discussed. More detailed information on LHCb design and operation can be found in [33].

2.1 The Large Hadron Collider

The **L**arge **H**adron **C**ollider (LHC) is the world's largest and most powerful particle accelerator. Located in the old LEP (Large Electron-Positron Collider) tunnel, about 100 m underground, at the European Organization for Nuclear Research (Conseil Européen pour la Recherche Nucléaire - CERN) near the city of Geneva. It started operating in 2008.

The LHC consists of a 27-km double ring synchrotron in which protons travel in opposite directions and are collided in eight interaction points, four of which correspond to the positions of the four major particle detectors - ATLAS, CMS, ALICE and LHCb. The other two experiments at LHC - LHCf and TOTEM - are located respectively near ATLAS and CMS.

Before entering the LHC rings, protons are produced and accelerated in 4 steps: they are obtained by ionization from hydrogen atoms and injected in bunches into the initial linear accelerator (LINAC2), which brings them up to an energy of 50 MeV, then they are fed through the Proton Synchrotron Booster (BOOSTER) which accelerates them

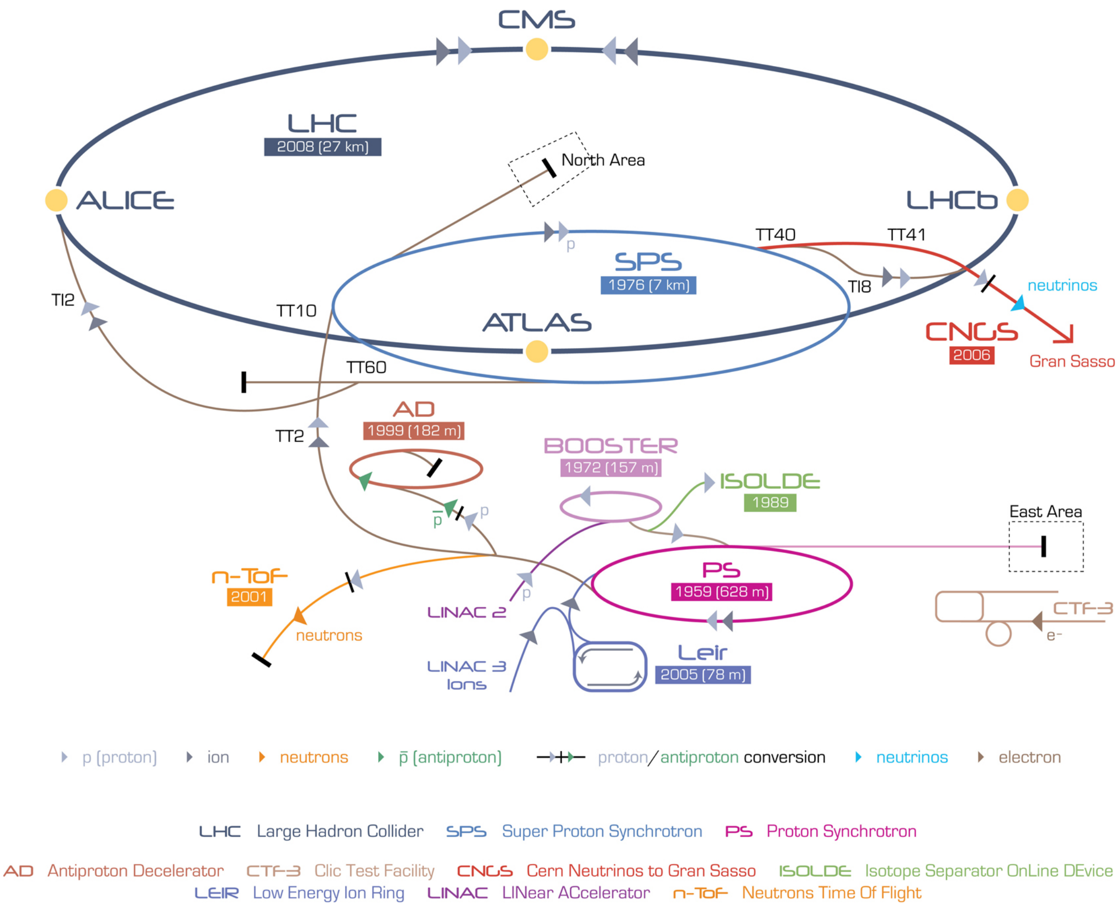

Figure 2.1: The LHC Accelerator Complex

up to 26 GeV, and finally are accelerated in the Super Proton Synchrotron (SPS), at an energy of 450 GeV before being injected into the LHC complex. Here, the maximum center-of-mass energy reached in 2013 was 8 TeV (13 TeV expected in 2015).

2.2 The LHCb detector

The production of $b\bar{b}$ couples has a large cross-section (see Figure 2.3) and its angular distribution is peaked in the forward and backward region as shown in Figure 2.2.
These characteristics suggest the design for the experiment as a spectrometer in the forward region; indeed LHCb's acceptance has an angular coverage from 15 mrad to 250 mrad vertically and 300 mrad horizontally, corresponding to the pseudo-rapidity region $1.6 < \eta < 4.9$. [1]

[1] Pseudo-rapidity is defined by $\eta = -ln(tan(\theta/2))$, θ being the angle between the particle momentum and the beam axis.

Circumference	27 km
Injection energy	450 GeV
Center of mass energy	14 TeV
Magnetic field at 2×450 GeV	0.535 T
Magnetic field at 2×7 TeV	8 T
Helium temperature	2 K
Instant luminosity	10^{34} $cm^{-2}s^{-1}$
Interbunch crossing time	25 ns
Stored energy (per beam)	362 $MJoule$

Table 2.1: The main design parameters of LHC

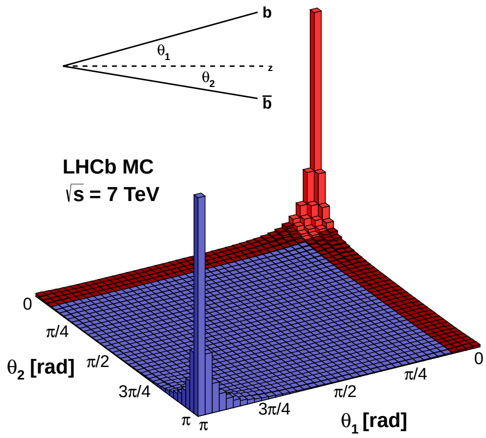

Figure 2.2: angular distribution of $b\bar{b}$ couples produced in pp collisions at LHC at $\sqrt{s} = 7TeV$. θ_b and $\theta_{\bar{b}}$ are the angles of the quarks momentum with respect to the beam axis.

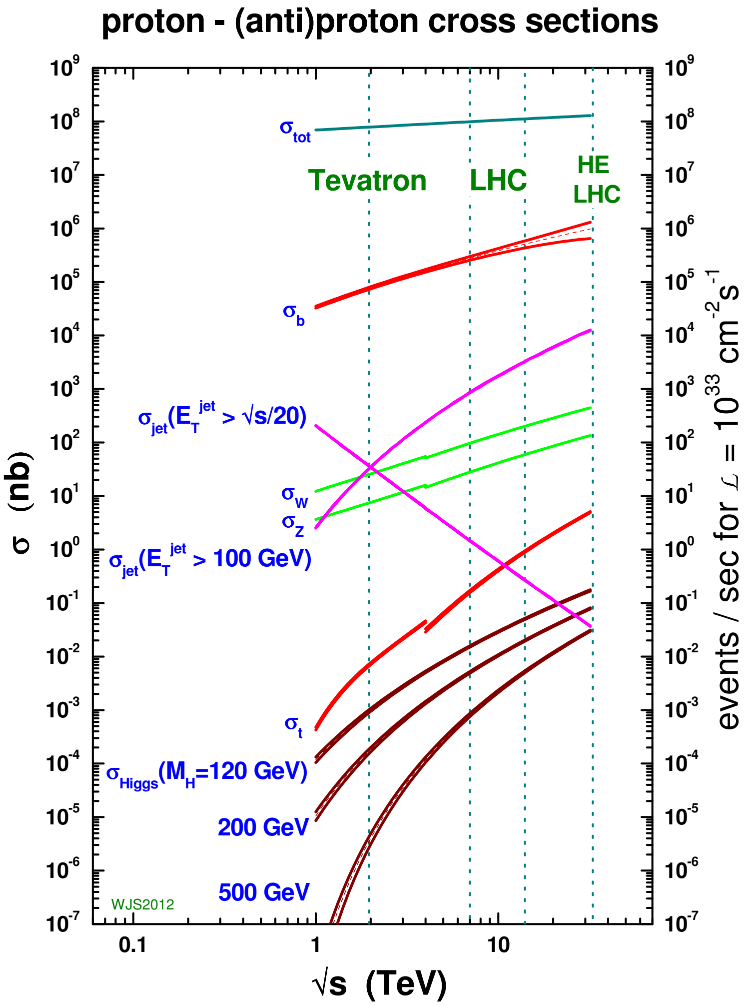

Figure 2.3: Standard model cross sections as a function of collider energy. These cross sections are calculated either at NLO or NNLO pQCD, using MSTW2008 (NLO or NNLO) parton distributions, with the exception of the total hadronic cross section which is based on a parametrisation of the Particle Data Group. The discontinuity in some of the cross sections at 4 TeV is due to the switch from proton-antiproton to proton-proton collisions at that energy.

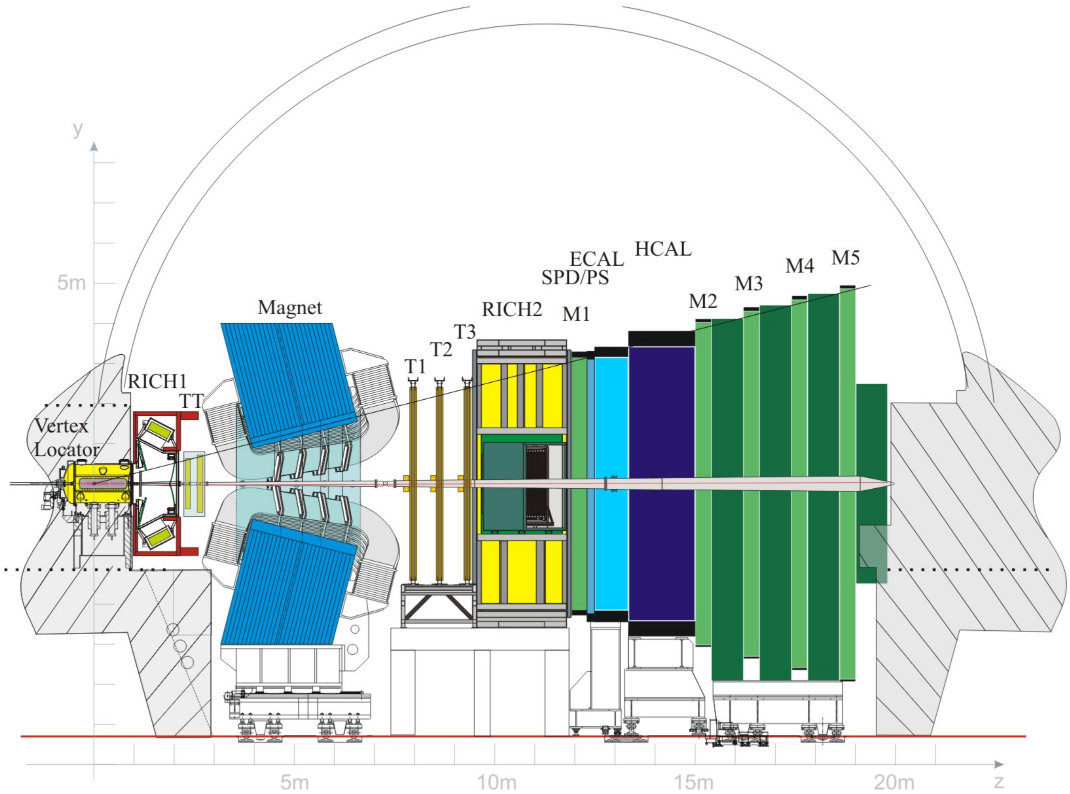

Figure 2.4: View of the LHCb detector.

LHCb does not run at the maximum LHC design luminosity: it works instead at the reduced luminosity of $2 \div 5 \times 10^{32} cm^{-2} s^{-1}$. This is achieved acting on the focusing and on the beam crossing area.
This choice is due to the crucial need for a precise vertex resolution. Indeed, the reconstruction of the point where the p-p collision took place, the *primary vertex*, and of the point where the produced particle decayed, the *secondary vertex* or *decay vertex*, is used to separate b decay products from particles produced directly at the p-p collision point and to reduce large prompt background. The possibility of detecting a B decay vertex would be negatively affected by the presence of multiple p-p interacions in the same bunch crossing (*in-time pile-up*). At the LHC design luminosity, on average 27 p-p collisions happen during each bunch crossing, on the contrary, at the LHCb reduced luminosity, collisions are dominated by a single or a few interactions; furthermore the occupancy in the detector remains low and radiation damage is reduced.

Figure 2.4 shows an overall view of the LHCb detector with its sub-detectors.

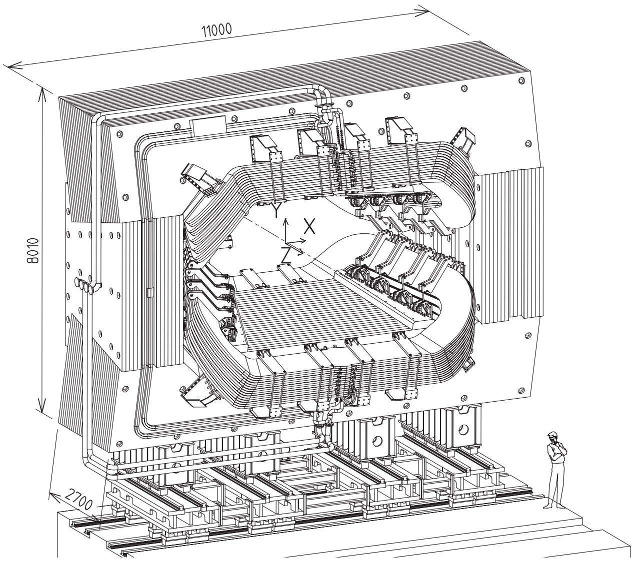

Figure 2.5: Perspective view of the LHCb dipole magnet. The interaction point lies behind the magnet.

2.2.1 Tracking detectors

The tracking system, for the above mentioned reasons is a crucial part of LHCb. It consists of a dipole magnet, a vertex locator system (VELO) and four planar tracking stations: the Tracker Turicensis (TT) upstream of the dipole magnet and three tracking stations T1, T2 and T3 downstream of the magnet, covering the entire spectrometer acceptance. VELO and TT use silicon microstrip detectors. In T1-T3, silicon microstrips are used in the region close to the beam pipe (Inner Tracker, IT) whereas straw-tubes are employed in the outer region of the stations (Outer Tracker, OT).

2.2.1.1 The magnet

A dipole magnet is used in LHCb to bend the tracks of charged particles, in order to measure their momentum.
It is a warm magnet, with saddle-shaped coils, placed mirror-simmetrically to each other in a window-frame yoke with sloping poles in order to match the required detector acceptance. The choice of this kind of magnet arises out of the need of balancing costs and performance [24].
With an integrated magnetic field of 4 Tm for tracks of 10 m length (i.e. tracks passing through the entire tracking system), it is possible for tracking detectors to perform momentum measurements for charged particles with a precision of about 0.4% for low momenta and 0.6% up to 200 GeV/c.

2.2.1.2 The Vertex Locator

To the purpose of identifying the displaced secondary vertices, the **Ve**rtex **Lo**cator (VELO) [26] provides precise measurements of track coordinates close to the interaction region; it consists of a series of circular silicon modules arranged along the beam direction as shown in Figure 2.6.
Each module is composed of two parts, providing respectively a measure of the r and φ coordinates. R sensors are segmented in concentric semi-circles, thanks to which it is possible to measure the distance from the z axis, while the φ sensors are segmented radially, for measuring the azimuthal angle. The third coordinate is provided by knowledge of the position of each sensor plane within the experiment.
Besides covering the entire forward acceptance of LHCb, the VELO does also partially cover the back hemishpere, in order to improve the identification of the primary vertex, while the first two R modules on the left form the pile-up veto system. To provide accurate measurements of the position of the vertices, the sensors are placed at a radial distance of about 8 mm from the beam axis, smaller than the aperture required by the LHC during injection and are therefore retractable. When closed, they slightly overlap; this is necessary for covering the full azimuthal acceptance and allows the reciprocal alignment.

The detectors are mounted in a vessel that maintains vacuum around the sensors, separated from the machine vacuum. This allows to minimize the material traversed by travelling particles. In order to evacuate the heat generated in the sensor electronics (in vacuum) and to minimize radiation-induced effects, the VELO is maintained at a temperature between -10 and $0°$C.

The sensors are 300 μm thick, radiation tolerant, built using the n-implants in n-bulk technology. To reduce the strip occupancy and pitch at the outer edge of the φ-sensors, the latter is divided in two parts: the outer region starts at a radius of 17.25 mm and has approximately twice the number of strips as the inner region.

The errors on the primary vertex position measurement arise mainly from the number of tracks produced in a pp collision. For an average event, the resolution in the z-direction is 42 μm and 10 μm perpendicular to the beam.

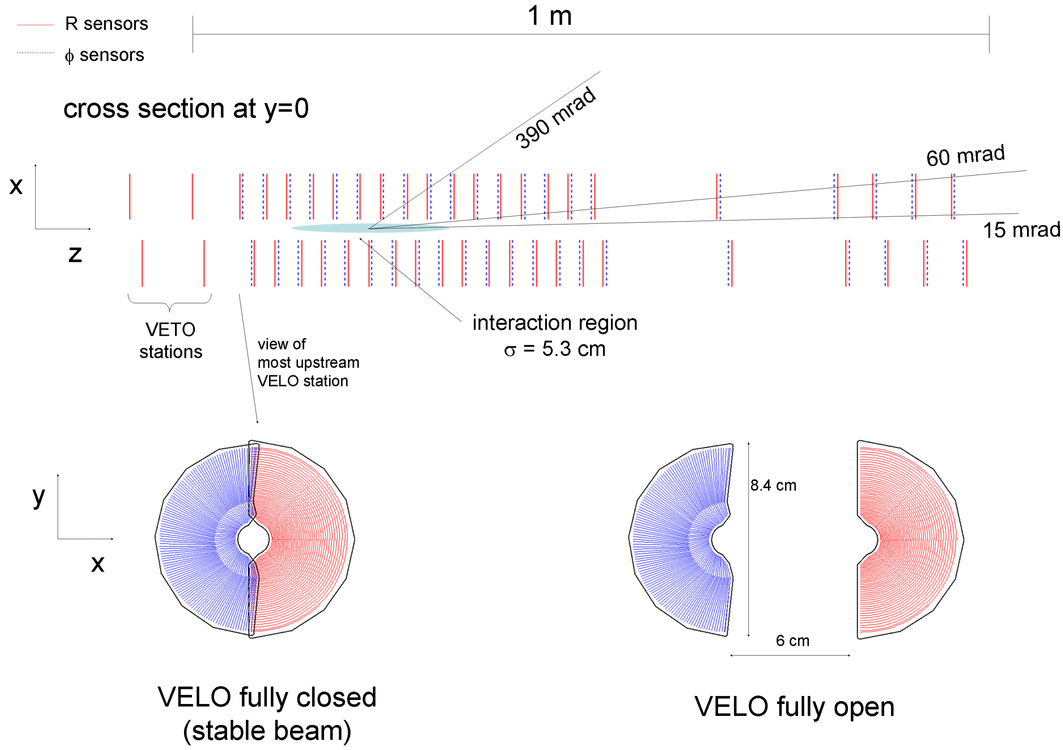

Figure 2.6: The setup of the VELO silicon modules along the beam direction. The indicated angles are: crossing angle for minimum bias events (60 mrad), minimal (15 mrad) and maximal (390 mrad) angle for which at least 3 VELO stations are crossed. 390 mrad is the opening angle of a circle that encloses a rectangular opening angle of 250 × 300 mrad. The front face of the first modules is also illustrated in both the closed and open positions.

2.2.1.3 The Silicon Tracker

The Silicon Tracker (ST) [30] comprises two detectors: the Tracker Turicensis (TT) and the Inner Tracker (IT). Both TT and IT use silicon microstrip sensors with a strip pitch of about 200 μm.

Tracker Turicensis Formerly known as the Trigger Tracker, the TT is a 150 cm wide and 130 cm high planar tracking station located upstream of the LHCb dipole magnet, covering the full acceptance of the experiment. It offers information for the HLT trigger and is used for track reconstruction.
Particles in the TT are bent by a magnetic field of about 0.15 T; this allows to improve the momentum estimation for the charged particles and provides tracking information for long-lived neutral particles which may decay outside the VELO.
The TT is composed of four layers covering the entire acceptance of the experiment, arranged in two pairs in an x-u-v-x configuration. The layout of the detector layers is

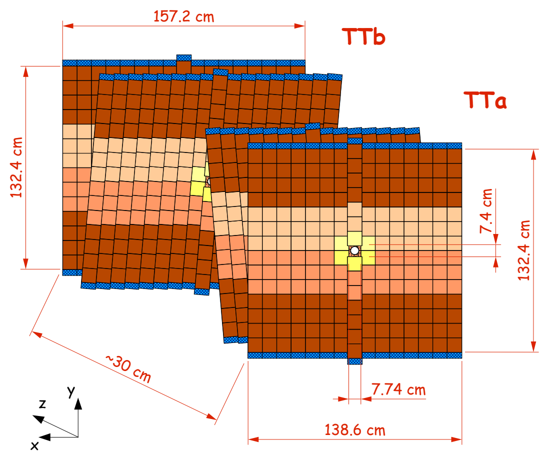

Figure 2.7: Layout of TT layers.

illustrated in Figure 2.7
The u and v layers are rotated around the z-axis to give the strips a stereo angle of $\pm 5°$ respectively. This arrangement provides sensitivity in the vertical (y) direction of the particle trajectories and helps improve track reconstructions.

Inner Tracker The Inner Tracker (IT) is a 120 cm wide and 40 cm high silicon microstrip detector installed in the centre of the tracking stations, close to the beam pipe. It performs accurate momentum estimates of the particles downstream of the magnet. The choice of silicon microstrip technology is due to the need of a fine detector granularity, necessary for managing the high track density in the region around the beam pipe. The IT is composed of 3 stations (T1, T2, T3), for each of which there are four detection layers in a similar x-u-v-x arrangement as for the TT. In order to obtain precise measurements in the bending (horizontal) plane and a sufficient resolution for tracks reconstruction in the vertical plane, a single 320 μm thick sensor is installed above and below the beam pipe, while double sensors of 410 μm are positioned along the sides of the beam pipe.
Figure 2.8 shows the layout of one of the IT layers.

2.2.1.4 The Outer Tracker

The Outer Tracker [28] covers the outer region of the three tracking stations T1-T3, surrounding the Inner Tracker; it performs track measurements downstream of the magnet, allowing to determine the momenta of charged particles.
Since the particle flux in this region is lower than in the IT, straw-tube detector techno-

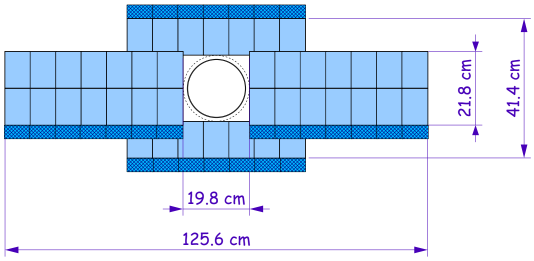

Figure 2.8: Layout of IT layers.

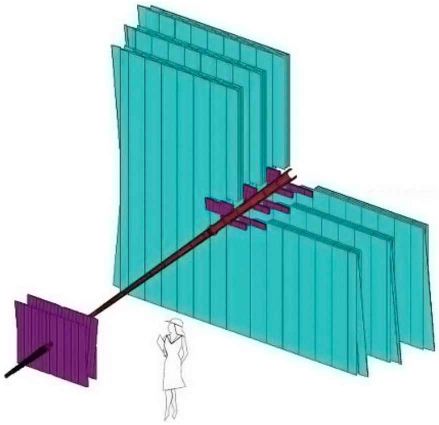

Figure 2.9: Configuration of the stations of the OT surrounding the IT (in purple).

logy is employed here. The Outer Tracker is indeed designed as an array of individual, gas-tight straw-tube modules, each containing two drift tubes. A combination of Argon (70%) and CO_2 (30%) is used. The front-end (FE) electronics measures the drift time of the ionization clusters produced by charged particles transversing the straw tubes and ionizing the gas.

The layout of the Outer Tracker is similar to that of the Inner Tracker and the Tracker Turicensis, arranged within the three tracking stations and consisting of four layers in the x-u-v-x arrangement, as shown in Figure 2.9 The external edge of the OT corresponds to an acceptance of 300 mrad horizontally and 250 mrad vertically.

2.2.2 Particle identification

Different types of charged particles (e, μ, π, K, p) travel through the detector, and must be distinguished. The information collected from the two RICH detectors, the calorimeters and the muon system collectively help to identify these particles.

Neutral particles such as photons and neutral pions, on the other hand, are identified using the electromagnetic calorimeter, where the $\pi^0 \rightarrow \gamma\gamma$ can be detected as either

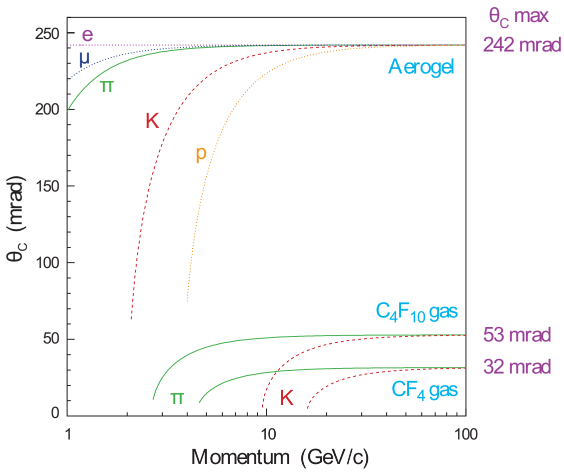

Figure 2.10: Relationship between θ_c and the momentum for different particles for the three media in the RICH.

two separate electromagnetic clusters (*resolved* π^0) or as a single one, resulting from the overlapping of the two clusters (*merged* π^0).

2.2.2.1 The RICH system

As in most particle physics experiments, K-π discrimination is a crucial task in LHCb. This task is performed by two **R**ing **I**maging **Ch**erenkov (RICH) detectors [25].
The upstream detector, RICH1, covers the low momentum charged particle range ($\sim 1 \div 60$ GeV/c) using aerogel and C_4F_{10} radiators, while the downstream detector, RICH2, covers the high momentum range from $\sim$ 15 GeV/c up to and beyond 100 GeV/c using a CF_4 radiator.
The procedure used for discrimination is as follows: the opening angle of the Cherenkov radiation cone allows to calculate the speed v of the particle as [44]

$$cos\theta_C = \frac{1}{n\beta} \tag{2.2.1}$$

where $\beta = v/c$, c being the speed of light in vacuum, and n is the refractive index of the medium.
Knowing the particle's momentum (from the tracking detectors) and its speed, it is then possible to determine its mass and use it to identify the particle. The relationship between θ_c and the momentum for different particles is shown in Figure 2.10. RICH 1 is situated between the VELO and the TT system, before the magnet and covers the full LHCb acceptance, while RICH 2 is located between the T3 station and the first muon station and has a more limited angular acceptance of $\pm$15 mrad to $\pm$120 mrad (horizontally) and $\pm$100 mrad (vertically). Their layout is shown in Figure 2.11.

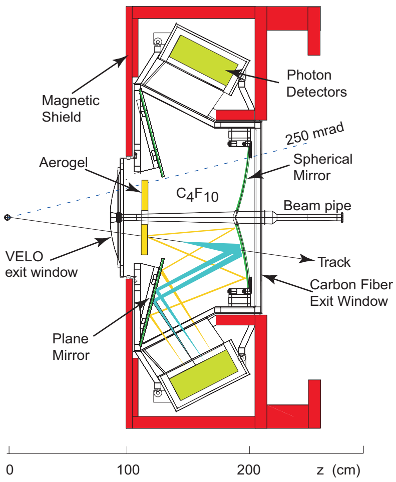

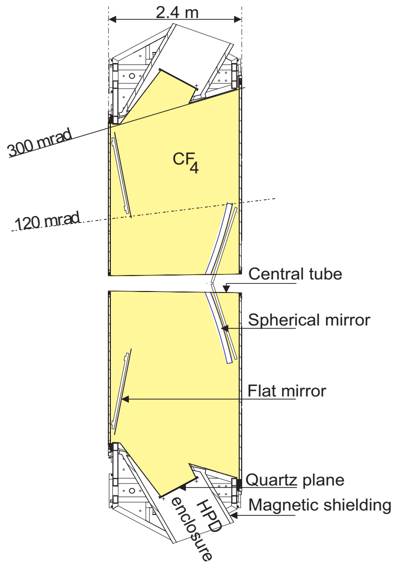

Figure 2.11: RICH1 (left) and RICH2 (right) detectors layout.

2.2.2.2 The calorimeter system

Located between the muon stations M1 and M2, the Electromagnetic Calorimeter (ECAL) and the Hadronic Calorimeter (HCAL) perform several functions. They select transverse energy hadron, electron and photon candidates for the first trigger level (L0), which responds $4\mu s$ after the interaction. Furthermore, they provide the identification of electrons, photons and hadrons as well as the measurement of their energies and positions. Reconstructing π^0s and prompt photons with good accuracy is essential for flavour tagging and for the study of B-meson decays.

Part of the calorimeter system [23] are also a Preshower detector (PS) and a Scintillator Pad Detector (SPD) plane, placed before the ECAL and separated from each other by a 15mm thick lead layer. They are mainly used for correctly identifying the electrons: the presence of the PS before the ECAL provides a longitudinal segmentation, necessary for discriminating charged pions, while the SPD allows to reject the background from high-E_T neutral pions.

The incident particles interact with the lead (in ECAL) or iron (in HCAL), creating a cascade of secondary particles. These particles hit the scintillators, which emit photons that are collected by photomultiplier tubes. The amount of light collected is proportional to the energy of the original incident particle.

Figure 2.12 shows the lateral segmentation for the different parts of the calorimeter system. The hit density variates with the distance from the bin, and thus the segmentation is not uniform.

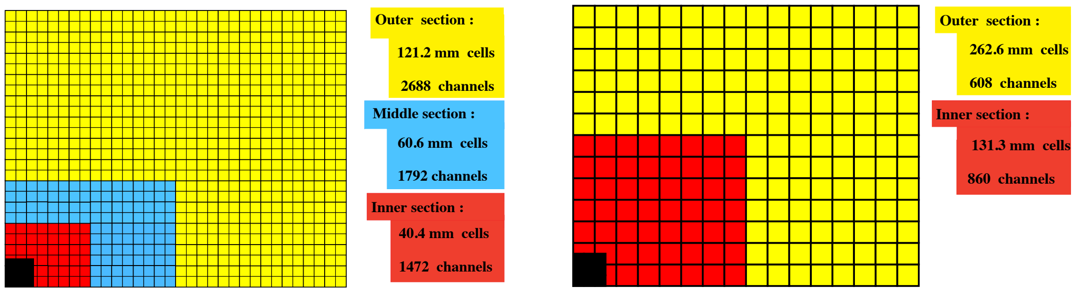

Figure 2.12: Lateral segmentation of the SPD/PS and ECAL (left) and of the HCAL (right). One quarter of the detector front face is shown. The cells dimensions in the left picture are given for ECAL and reduce by $\sim 1.5\%$ for SPD/PS.

2.2.2.3 The muon system

The muon system of the LHCb experiment [27] consists of five rectangular tracking stations placed along the beam axis. The first station (M1) is placed upstream of the calorimeter preshower, while the remaining four stations (M2, M3, M4 and M5) are located downstream of the calorimeter, interleaved with iron absorbers to select penetrating muons. Figure 2.13 shows a side view of the system.

The inner and outer angular acceptances of the muon system are 20 (16) mrad and 306 (258) mrad in the bending (non-bending) plane respectively. This results in an acceptance of about 20% for muons from inclusive b semileptonic decays.

Stations M1–M3 have a high spatial resolution along the x coordinate (bending plane). They are used to define the track direction and to calculate the p_T of the candidate muon, while stations M4 and M5 have a limited spatial resolution, their main purpose being the identification of penetrating particles.

Each station is subdivided in four regions with dimensions and segmentation scaling as 1:2:4:8, so that the particle flux and channel occupancy are roughly the same.

In the muon stations multi wire proportional chambers are used, operating with a gas mixture of Ar (45%), CO2 (15%) and CF4 (40%), with the exception of the inner part of the most upstream station where GEM (Gas Electron Multiplier) chambers are installed.

2.2.3 Data treatment

The LHCb trigger system [31] is subdivided in a low level pure hardware part and a high level software part.

The events surviving to the triggering are submitted to a preliminary reconstruction that classifies the events, through a flag assignment, according to their specific characteristics as, for example, the presence of a couple of muons forming the J/ψ, or being compatible with specific b or c quark decays of interest. This procedure is called *stripping*.

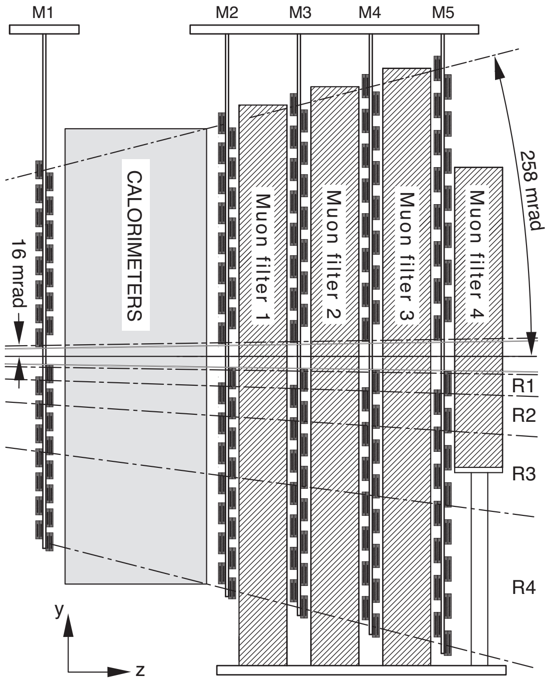

Figure 2.13: Side view of the muon system.

The numerous LHCb computing tools used for offline analysis and simulation are described in details in [32].

2.2.3.1 The trigger

Due to the LHC bunch structure and low luminosity, the crossing frequency with interactions visible[2] by the spectrometer is about 10 MHz, which has to be reduced by the trigger to about 2 kHz for being written to storage for further offline analysis. The LHCb trigger is divided in two different levels (see Figure 2.14):

- the first level, called Level-0 (L0), is a hardware trigger, implemented using custom made electronics synchronously operating with the 40 MHz bunch crossing frequency, to reduce the input rate to a maximum of ∼1 MHz. At this rate, the whole detector can be read out.
  The L0 trigger receives information from three subsystems: the calorimeter trigger, the muon trigger and the pile-up trigger and it identifies the highest ET hadron, electron and photon clusters in the calorimeters and the two highest p_T muons in the muon chambers;

[2]An interaction is defined to be visible if it produces at least two charged particles with sufficient hits in the VELO and T1–T3 to allow them to be reconstructible.

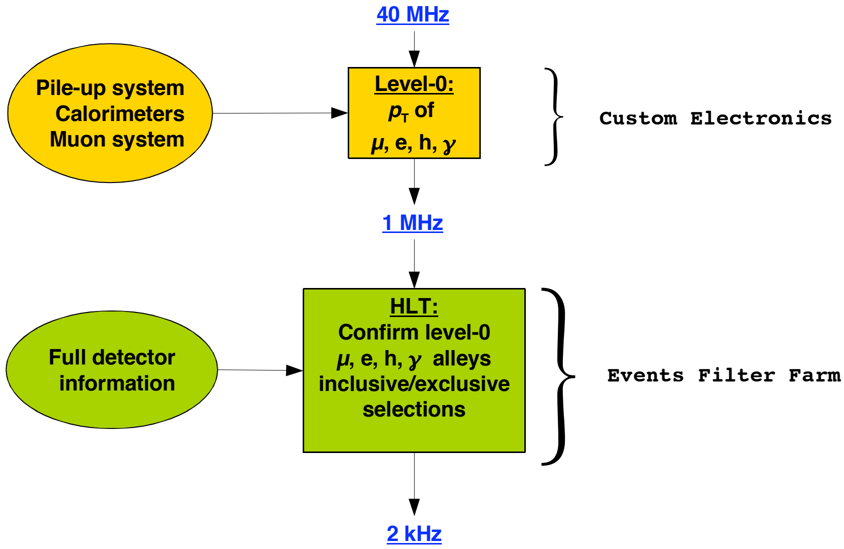

Figure 2.14: A sketch of the trigger system.

- the High Level Trigger (HLT) is a C++ application running on an Event Filter Farm [29] composed of several thousands CPU nodes. It receives the L0 output and reduces the rate to a maximum of about 3 kHz, sending its output directly to storage. The HLT is subdivided in two stages, HLT1 and HLT2.
  HLT1 performs the so-called *Level-0 confirmation*. Namely, it reconstructs particles in the VELO and T-stations corresponding to the L0 objects, or in the case of γ and π^0 candidates, it checks the absence of a charged particle which could be associated to these objects. At the HLT2 level, events are reconstructed and selected by a set of inclusive and exclusive algorithms.
  At this stage, selection cuts are relaxed compared to the offline analysis. This is done in order to be able to perform later sensitivity studies and to profit from refinements due to improvements in the calibration. A large fraction of the output bandwidth is devoted to calibration and monitoring.

In order to monitor efficiencies and systematic uncertainties both trigger levels can be emulated fully on stored data.

2.2.3.2 Track reconstruction

The hits in the VELO, the TT, the IT and the OT detectors are combined by the track reconstruction software to form particle trajectories from the VELO to the calorimeters. The reconstruction algorithm aims at finding all tracks in the event which leave sufficient detector hits.
Depending on their trajectories inside the spectrometer, the tracks are classified in the

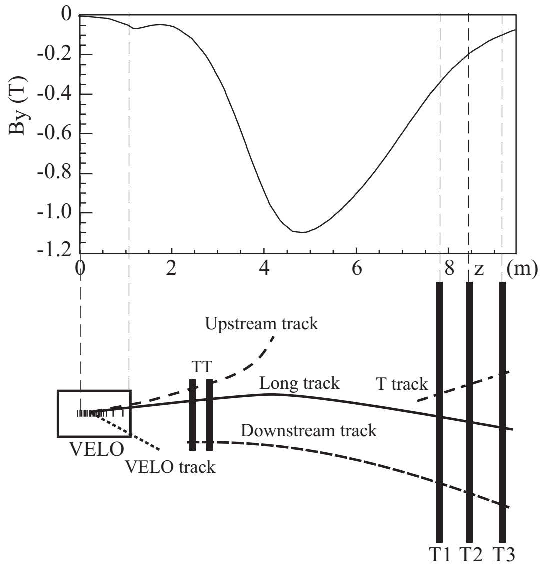

Figure 2.15: A schematic illustration of the various track types: long, upstream, downstream, VELO and T tracks. The main B-field component (By) is plotted above as a function of the z coordinate.

following categories, as illustrated in Figure 2.15:

- **long tracks**: these are the tracks that go through the entire tracking set-up from the VELO to the T stations. These are the most important set of tracks for b-hadron decay reconstruction, having the most precise momentum determination;
- **upstream tracks**: these tracks traverse only the VELO and the TT stations. Upstream tracks have in general lower momentum and are bent out of the detector acceptance by the magnetic field;
- **downstream tracks**: transversing only the TT and T stations, these tracks are not seen in the VELO. They are mostly originated from products of K^0_S and Λ decaying outside the VELO acceptance;
- **VELO tracks**: as against to the latter, these tracks are only seen in the VELO. They are typically large angle or backward tracks, useful for the primary vertex reconstruction;
- **T tracks**: only measured in the T stations, these tracks are tipically produced in secondary interactions, but are useful for the global pattern recognition in RICH2.

Further information on track reconstruction can be find in [33] and [48].

2.2.3.3 Monte Carlo

A key ingredient of data analysis in particle physics is the study of data simulated with the Monte Carlo (MC) method.
This allows to improve the knowledge of what one should expect from an experiment. In particular it is often used for studying the background of a given signal, for calculating properties of the selection chain such as efficiency and purity and for *training* some software tools that are later used on data.

In LHCb, MC simulations are generated by the application Gauss [55], which consists of a collection of libraries for physics simulation based on the Gaudi framework [1]. It generates the physical process of interest through the PYTHIA [52] generator package, that simulates the physics inherent the p-p interaction and the hadronization process. PYTHIA has been specifically tuned to reproduce the correct track multiplicities in the LHCb acceptance. The physics of b decays is handled by a specific package, called EvtGen, originally developed for the experiments BaBar and Cleo. EvtGen is able to simulate many different types of decays [22].
The detector response is simulated in a second stage with the GEANT4 [2] package, taking into account a very precise description of the detector geometry and the detail of the physic processes behind the operation of each subdetector.

Chapter 3

Data Analysis

This chapter describes the logical flow and the techniques used in the present analysis: the main operations that have been performed are discussed in detail and their effects are shown.

The analysis to reconstruct the decay chain $B^+ \to J/\psi(\to \mu^+\mu^-)\ \omega(\to \pi^+\pi^-\pi^0)\ K^+$ and its charge conjugate[1] starts from events flagged by the stripping line

StrippingFullDSTDiMuonJpsi2MuMuDetachedLine,

described in detail in 3.2.1, and it consists of the following operations:

1. **Decay chain reconstruction**: this process, described in 3.2.3, Section consists of combining the reconstructed particles to form candidate signal events responding to specific requirements mainly related to the decay's kinematic. At this stage, the applied cuts are very loose. The output of this first step is a so called *n-tuple*, i.e. a ROOT [6] object containing all the necessary information organized by event and by particle. At this stage a *kinematic re-fit* is also performed, which will be described later.

2. **Preselection**: a further set of cuts, described in detail in 3.2.4, is performed in order to get rid of those events which are most easily identifiable as background. The cuts chosen here must be highly efficient on signal, in order not to loose precious events, but at the same time they provide significant background suppression.

3. **MVA**: a Multivariate Analysis (see 3.3) is then applied as a finer selection. This algorithm combines a set of discriminating variables, chosen conveniently by the user, in order to build a new variable which provides an optimal signal-background discrimination. Cutting on this variable will then provide both high signal efficiency and background rejection.

[1]Hereinafter, both the B^+ decay and its charge conjugate are always meant to be taken into account.

4. **sPlot**: the obtained B mass spectrum is fitted with an appropriate Probability Density Function (PDF) consisting of a signal and a background component. As explained in 3.5,once this fit is performed, the sPlot technique is applied: to each event two weights are ascribed, proportional respectively to the signal and to the background PDF evaluated in the mass corresponding to the event. For a detailed description of this technique cf. Appendix A. This procedure allows to obtain background-subtracted distributions of the variables of interest, such as the $J/\psi\ \omega$ invariant mass, in this case.

5. **Efficiency correction**: a last step is necessary in order to correctly reproduce the true signal. All the selections applied up to this point obviously entail an efficiency loss which, in principle, is not even constant in the whole $J/\psi\ \omega$ invariant mass spectrum. The overall efficiency must therefore be calculated from the Monte Carlo sample and then used to correct our data. This procedure is described in detail in 3.7.

3.1 Data and Monte Carlo samples

In the present analysis the full 2011 + 2012 data sample is used, corresponding to an integrated luminosity of $\sim 1fb^{-1}$ (2011) $+2fb^{-1}$ (2012) of $p-p$ collision data, recorded with the LHCb detector at a centre of mass energy of 7 TeV for 2011 data and 8 TeV for 2012 data.

Two MC samples are used:

- A simulation consisting of 2 million events reproducing the 2011 data taking conditions and 4 million events for the 2012 data taking conditions. Here the full detector simulation is applied and the event reconstruction identical as to real data is performed.
- A control sample composed of 40000 events in the full spectrum. In this sample only the EvtGen output is stored, i.e. no GEANT4 simulation is performed. The LHCb geometrical acceptance cut is applied to the B daughters.

Both sample simulate the decay chain

$$B^+ \to (J/\psi \to \mu^+\mu^-)\ (\omega \to \pi^+\pi^-\pi^0)\ K^+ \tag{3.1.1}$$

as a Phase Space three body decay.
The two MC samples are stored as ntuples containing the reconstructed events (for the

Candidate	**Variable**	**Cut**
	P_T	$> 500\ MeV/c$
μ	$DLL_{\mu\pi}$	> 0
	Track χ^2/N_{dof}	< 5.0
	$M(\mu\mu)$	$\in [2996.916, 3196.916]\ MeV/c^2$
J/ψ	DLS	> 3.0
	χ^2_{DV}/N_{dof}	< 5.0

Table 3.1: Stripping line selection cuts.

first sample only) and the so-called *MC truth*, that is the events as they were simulated, with the original four-momenta vectors without any reconstruction effect simulation.

3.2 Event selection

3.2.1 Stripping

As mentioned above, the *stripping line* used for the present analysis is called *Stripping-FullDSTDiMuonJpsi2MuMuDetachedLine*. It aims at reconstructing decays originating from a B meson and containing a $J/\psi \rightarrow \mu^+\mu^-$. The algorithm selects events with a detached secondary vertex formed by combining two muon tracks with opposite charge and moderate transverse momentum. This is required because the B meson travels for a measurable distance before decaying.
During this procedure some loose cuts are applied, shown in Table 3.1

To be more sure that the selected track actually corresponds to a muon, a cut on the Delta Log Likelihood (DLL) $\mu - \pi$ is applied. The DLL variables are used for Particle Identification (PID). They indicate the difference of the logarithm of the likelihood fit of a certain identification hypothesis with respect to the pion hypothesis, calculated using information from each detector subsystem. For example, in the case of $DLL_{\mu\pi}$ the difference between the muon and the pion case is computed:

$$DLL_{\mu\pi} = log(\mathcal{L}_\mu) - log(\mathcal{L}_\pi) = log(\frac{\mathcal{L}_\mu}{\mathcal{L}_\pi}) \tag{3.2.1}$$

The two muon tracks need to originate from the same vertex, and this is checked with a cut on the J/ψ Decay Vertex (DV) χ^2 per degree of freedom, χ^2_{DV}/N_{dof}. Furthermore, in order to select good muon tracks, a cut on the track's χ^2/N_{dof} is performed. Aiming at selecting detached J/ψ vertices a cut on the Decay Lenght Significance (DLS, defined as the distance between the reconstructed $\mu^+\mu^-$ vertex and the PV, divided by its error) is applied. The dimuon invariant mass is required to be in a 200 MeV/c^2 wide window centered in the nominal J/ψ mass. Finally, a lower cut of $550 MeV/c$ on the muon momentum is applied.

3.2.2 MicroDST

DST[2] files contain huge amounts of data, making their handling quite demanding in terms of computing power. For these reasons they undergo a set of further loose selections which create many different subsamples, called *MicroDSTs*, each for a different kind of decay which contain only the information strictly needed for the specific analysis.
In our case, the decay $B^+ \to J/\psi\ \omega\ K^+$ and its charge conjugate are selected via the cuts listed in Table 3.2.
Those cuts mainly involve tranverse momenta, invariant masses, pseudo-rapidity intervals, χ^2 of tracks and vertices, and particle identification variables.
A cut on the lifetime of the B meson is also applied, along with cuts on the χ^2 distance between tracks of daughter particles of the B and of the ω (Min. χ^2 dist.).
A contribution to our final state could be actually also provided by the decay $B^+ \to J/\psi\ \eta\ K$ which is, however, eliminated by the cut on the three pions invariant mass of $\pm 100\ MeV/c^2$ around the nominal ω mass.

3.2.3 Decay chain reconstruction

In order to reconstruct the full decay chain, each J/ψ candidate needs to be associated with two opposite charge pions, a neutral pion and a charged kaon. These are collected from the LHCb *StandardParticles* repository: here the particle candidates are subject to some loose cuts.
The standard algorithms used in the reconstruction are, in particular, *StdLoosePions*, *StdLooseKaons*, *StdLooseMuons*, *StdLooseResolvedPi0*.
In the first three mentioned algorithms, a cut on the particles' transverse momentum is applied ($P_T > 200\ MeV/c$). Mention should be made of the fact that, for muons, this cut is actually lower than the one applied in the stripping phase. Also the χ^2 of the fit of the charged track Impact Parameter ($\chi^2(IP) > 4.0$) is applied, aiming at removing the background composed of prompt particles.
In *StdLooseResolvedPi0* a photon pair with $P_T(\gamma) > 200$ MeV/c and $M(\gamma\gamma) \in [85, 185]$ MeV/c^2 is combined to form a π^0. Each photon pair is required to be resolved i.e. the two photons must be associated to two distinct clusters in the electromagnetic calorimeter. (cf. 2.2.2).
After an additional cut on the track fit χ^2, pions are combined to reconstruct an ω

[2]Date Summary Tapes: this is the file format used to store data.

Candidate	**Variable**	**Cut**
$\mu^{\pm}$	P_T	$> 550\ MeV/c$
	$DLL_{\mu\pi}$	> 0
	Tr. Clone Dist.	> 5000
$\pi^{\pm}$	P_T	$> 200\ MeV/c$
	Tr. Clone Dist.	> 5000
	Tr. Ghost Prob.	< 0.5
	Tr. χ^2/N_{dof}	< 4
	η	$\in [2, 5]$
	P	$\in [3.2, 150]\ GeV/c$
	Has Rich Info	true
	ProbNNpi	> 0.1
	IP χ^2/N_{dof}	> 4
π^0	$\min(P_T)$	$> 250\ MeV/c$
K^+	P_T	$> 200\ MeV/c$
	Tr. Clone Dist.	> 5000
	Tr. Ghost Prob.	< 0.5
	Tr. χ^2/N_{dof}	< 4
	η	$\in [2, 5]$
	P	$\in [3.2, 150]\ GeV/c$
	Has Rich Info	true
	ProbNNk	> 0.1
	IP χ^2/N_{dof}	> 4
ω	$M(\pi^+\pi^-)$	$< 1\ GeV/c^2$
	Min. χ^2 Dist. $(\pi^+\pi^-)$	< 12
	$P_T(\pi^+\pi^-\pi^0)$	$> 0.63\ GeV/c$
	$\lvert M(\pi^+\pi^-\pi^0) - M_{\omega}^{PDG}\rvert$	$< 100\ MeV/c^2$
	Vertex χ^2	< 9
	P_T	$> 0.7\ GeV/c$
J/ψ	$\lvert M(\mu^+\mu^-) - M_{J/\psi}^{PDG}\rvert$	$< 120\ MeV/c^2$
	Vertex χ^2	< 20
γ	P_T	$> 250\ MeV/c$
B^+	$M(J/\psi\omega)$	$< 7\ GeV/c^2$
	Max χ^2 Dist. $(J/\psi\omega)$	< 20
	Vertex χ^2/N_{dof}	< 10
	$c \cdot \tau$	$> 100\ \mu m$
	$M(J/\psi\omega K)$	$\in [4.55, 6.70]\ GeV/c^2$

Table 3.2: MicroDST cuts.

Candidate	**Variable**	**Cut**
γ	P_T	$> 200\ MeV/c$
$\pi^{\pm}$	IP χ^2/N_{dof}	> 4
	P_T	$> 200\ MeV/c$
	Track χ^2/N_{dof}	< 4
π^0	P_T	$> 200\ MeV/c$
	$M(\gamma\gamma)$	$\in [85, 185]\ MeV/c^2$
K^+	IP χ^2/N_{dof}	> 4
	P_T	$> 200\ MeV/c$
ω	χ^2_{DV}/N_{dof}	< 20
	$M(\pi^+\pi^-\pi^0)$	$\in [390, 1000]\ MeV/c^2$
	P_T	$> 1\ GeV/c$
J/ψ	$M(\mu^+\mu^-)$	$\in [3040, 3140]\ MeV/c^2$
	P_T	$> 1.5\ GeV/c$
	χ^2_{DV}/N_{dof}	< 20
B^+	P_T	$> 1.5\ GeV/c$
	χ^2_{DV}/N_{dof}	< 15
	$c \cdot \tau$	$> 60\ \mu m$
	$\lvert M(J/\psi\omega K) - M_B^{PDG}\rvert$	$< 500\ MeV/c^2$

Table 3.3: Reconstruction cuts, including the StandardParticles cuts.

meson.
A tighter cut compared to that in the stripping is applied on the J/ψ mass. This cut is not symmetric, in order to take into account the radiative tail. The transverse momentum of the J/ψ is also cut again.
The invariant mass of the system $J/\psi\ \omega K$ is required to fall in a 1000 MeV/c^2 wide symmetric range around the nominal $B^{\pm}$ mass, an upper cut on the χ^2 of their common vertex is applied and another cut on the transverse momentum of the B is performed.
Finally, a lower cut on the B meson's lifetime is applied in order to reject the combinatorial background.
All the cuts are listed in Table 3.3.

The full decay chain is at this point submitted to kinematic re-fits that constrain some properties of the particles to their nominal values. In particular, three different sets of variables (branches of the ROOT TTree) are produced for each candidate, which we will refer to as set I, II and III:

- **set I**: branches with re-fit with constrained J/ψ mass;
- **set II**: branches with re-fit with constraints applied to the J/ψ and π^0 masses and

to the Primary Vertex Pointing (PVP);

- **set III**: branches with re-fit constraints applied to the J/ψ and π^0 masses, to the Primary Vertex Pointing (PVP) and to the B mass.

The momenta of all the particles of the decay chain are readjusted to match with the requirements imposed by the fixed invariant masses. Similarly, the Primary Vertex Pointing condition imposes that the B momentum is aligned with the vector formed by the primary and the B decay vertices.

The idea behind the re-fit procedure is that if an event is actually a signal event, some of its characteristics are known and constraining them to their nominal values should improve the resolutions of the other variables with which the constrained ones are correlated.
The re-fit can of course fail for some events; in this case a non-physical value is assigned to the respective variables and subsequently those events are rejected during the later steps of the analysis, when considering the corresponding variables. In principle, the failure of the re-fit indicates that the event is somehow not compatible with the signal's kinematic, i.e. it acts as a filter to reject background.

3.2.4 Preselection cuts

The preselection consists of a last set of cuts, shown in Table 3.4, which eliminates obvious sources of background, according to LHCb fiducial cuts, that are highly efficient on signal and assure a significant background rejection.

In addition to the kinematic variables considered in the previous cuts, this step of the selection involves some other quantities, such as the Confidence Level (CL), calculated from the DLL values, which assures a good quality ID of the photons from the neutral pion. The variable ranges from 0 to 1 and, in the case of the photon, takes into account information about the cluster size, the shower shape and the energy deposit in the Scintillating Pad Detector in front of the calorimeter. The CL of the π^0 is the product of the two photons' CLs.
A *ghost track* is defined as a pseudo-random combination of hits, and it is characterized by having a low χ^2 from the track fit and missing hits. Such a track, therefore is not associated to any real particle: it's merely a result of hit combination mistakes. A specialized algorithm determines a probability for each track to be a ghost.
Min. IP χ^2 refers to the minimum χ^2 of the track with respect to any primary vertex. This cut is performed in order to remove a significant fraction of background composed of prompt particles.

Candidate	Variable	Cut
$\mu^{\pm}$	is Muon	true
	P	$> 0\ MeV/c$
	P_T	$> 1000\ MeV/c$
	$PID\mu$	> 0
	Min. IP χ^2	> 9
	Track χ^2/N_{dof}	< 4
	Tr. Clone Dist.	> 5000
	Tr. Ghost Prob.	< 0.4
$\pi^{\pm}$	Tr. Clone Dist.	> 5000
	Min. IP χ^2	> 9
	P_T	$> 200\ MeV/c$
	Track χ^2/N_{dof}	< 4
	PIDK	< 0
	Tr. Ghost Prob.	< 0.4
π^0	P_T	$> 200\ MeV/c$
	C.L.	> 0.01
	$M(\gamma\gamma)$	$\in [85, 185]\ MeV/c^2$
K	Tr. Clone Dist.	> 5000
	Min. IP χ^2	> 9
	P_T	$> 200\ MeV/c$
	Track χ^2/N_{dof}	< 4
	PIDK	> 0
	Ghost Prob.	< 0.4
ω	χ^2_{DV}/N_{dof}	< 20
	$M(\pi^+\pi^-\pi^0)$	$\in [400, 1000]\ MeV/c^2$
	P_T	$> 2000\ MeV/c$
J/ψ	$M(\mu^+\mu^-)$	$\in [3040, 3150]\ MeV/c^2$
	P_T	$> 2000\ MeV/c$
	χ^2_{DV}/N_{dof}	< 9
B	Re-fit III χ^2/N_{dof}	> 0
	$c \cdot \tau$	$> 75\ \mu m$
	P_T	$> 2000\ MeV/c^2$
	$\lvert M^{reco}(B) - M^{PDG}(B)\rvert$	$< 500\ MeV/c$
	$\chi^2_{DV}/Ndof$	< 12

Table 3.4: Preselection cuts.

Clone Dist. refers to the Kullback-Liebler distance [47], that is a quantity which measures the difference in information content between two tracks. Two tracks are called clones if they provide the same information. If two or more tracks have small values of this distance, the one with better quality is identified, and the others are tagged with the value of this distance with respect to it. This cut, thus, aims at rejecting clone tracks. Cuts are also applied on the Delta Log Likelihood variables used for the Particle Identification.

3.3 Multivariate Analysis

The Multivariate Analysis is a statistical technique used to analyse and discriminate data coming from two different sources (signal and background). It consists of an algorithm that receives as input a set of variables conveniently chosen for their discriminating power and produces as output a unique variable in which signal and background are optimally separated.
This kind of analysis consists of two steps.

1. The first one is the so-called *training phase*. Here the user provides the signal (S) and background (B) data samples. The tool applies the discrimination procedure, based on the input variables, and produces an output file (*weights file*) containing all the information extracted, namely the mapping function that will allow to discriminate the events.

2. The second step is the *classification*: in this phase the signal-background discrimination information, retrieved from the weights file, here taken as input, is used on the data sample in order to discriminate the events: for each event a value of the new discriminating variable is computed.

The selection will then consist of a simple cut on this variable.

In the case of the present analysis the S dataset is represented by the signal MC simulation, while B consists of the real data in the B^+ mass sidebands $|M^{reco}(B^+) - M^{PDG}(B^+)| > 150\ MeV/c^2$.

The output variable can be obtained with different statistical methods. The one used in the present analysis is the Projective Likelihood Estimator (PLE). This method requires the input variables being uncorrelated or at least, in a more realistic case, weakly-correlated.
PLE represents the optimum choice mainly for two reasons:

- it provides the best signal-background separation, under the hypothesis of the PDFs' modelling being accurate. Inaccuracies can be due to imprecisions in the interpolations or unwanted input variables correlations;
- both the training and the application of the likelihood classifier are relatively fast operations in terms of CPU time.

For each event i, the likelihood for it belonging to signal type is the product of all signal PDFs evaluated at the measured variable value, and conveniently normalized. Thus, for the signal:

$$\mathcal{L}_S(i) = \prod_{k=1}^{M} p_S^k(x_k(i)) \tag{3.3.1}$$

and, similarly, for the background:

$$\mathcal{L}_B(i) = \prod_{k=1}^{M} p_B^k(x_k(i)) \tag{3.3.2}$$

where p_S^k and p_B^k are respectively the signal and background PDFs for the k^{th} input variable x_k, and M is the number of input variables. Each PDF is normalized to 1, for every x_k.

This factorization of the total PDF is only legitimate in case of non-correlated variables: here lies the reason why a negligible correlation between the input variables is needed; the more these are correlated, the less accurate the result will be.

The ratio

$$r_{\mathcal{L}}(i) = \frac{\mathcal{L}_S(i)}{\mathcal{L}_S(i) + \mathcal{L}_B(i)} \tag{3.3.3}$$

is the variable used to discriminate between S and B hypotheses. As above-mentioned, this quantity is known to be the most powerful discriminating variable (Neyman-Pearson lemma, [50]).

The MVA procedure is performed in this analysis using the Toolkit for Multivariate Data Analysis (TMVA) [43], provided by the ROOT framework.

3.3.1 Training phase

An accurate choice of the input variables is essential at this point.

The distributions for signal and background of all the available variables have been checked and six of them have been chosen basing on the above-mentioned requirements and on their discriminating power (in some cases the logarithm is taken, in order to smooth the distributions):

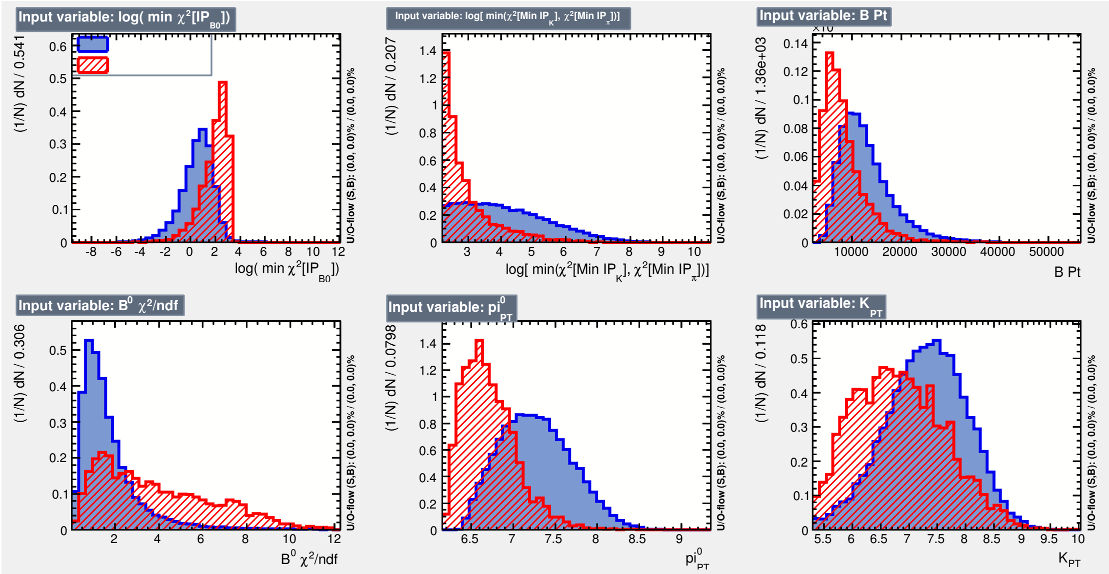

Figure 3.1: Signal and background distributions for the MVA input variables.

- $log(min(\chi^2(IP_B))$: the logarithm of the minimum reduced χ^2 of the B^+ Impact Parameter with respect to all Primary Vertices in an event. A signal B^+ must come from a PV, and so the IP (i.e. the perpendicular distance between the B^+ reconstructed momentum vector and the PV) should be small, with a good χ^2. The signal distribution for this variable presents indeed a peak at zero, far below the background distribution peak.

- $log(min(\chi^2(MinIP_K), \chi^2(MinIP_\pi))$: the logarithm of the minimum IP reduced χ^2 with respect to all PVs and with respect to all charged hadrons in the final state (K, π^+ and π^-). Since these particles must come from a detached vertex, their IP χ^2 is expected to be peaked at a greater value than zero, while the background is composed mainly of prompt particles with low IP χ^2.

- B_{PT}: the B^+ transverse momentum. Signal B mesons' PT is peaked at $\sim 10\ GeV/c$, while background candidates have lower transverse momentum.

- $\chi^2_{DV}/N_{dof}(B)$: the reduced χ^2 of the decay vertex fit of the B^+. This variable has a signal peak around 1, corresponding to the vertices that have been well reconstructed from the charged tracks of muons, pions and the kaon. This situation of good vertices is, of course much less frequent for the background.

- $log(\pi^0_{PT})$ the π^0 transverse momentum. Signal neutral pions coming from a B^+ decay present a peak for larger values and a longer distribution tail towards high transverse momenta than π^0s produced in the pp interaction.

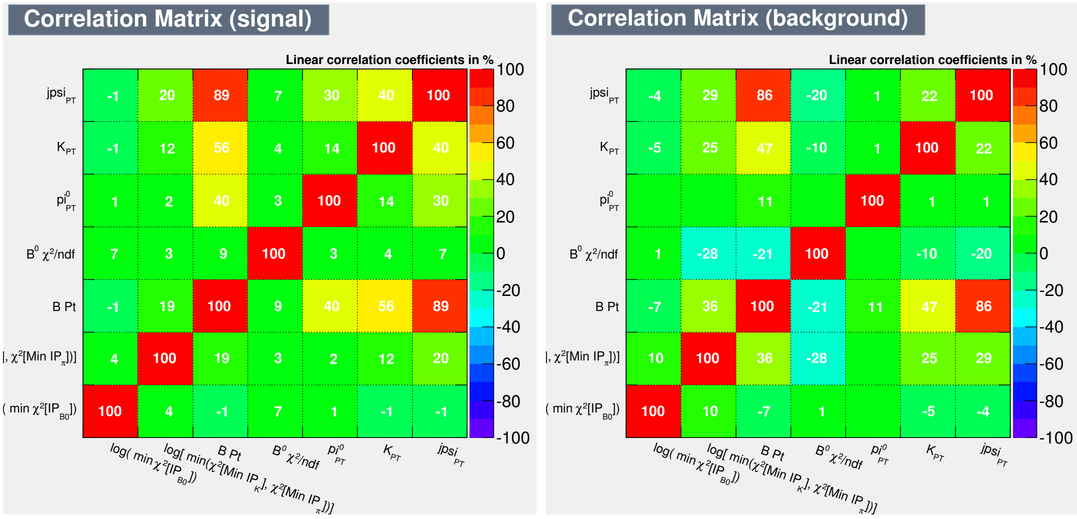

Figure 3.2: Correlation matrices for signal and background samples.

- $log(K_{PT})$ the K transverse momentum. As for the π^0, the signal kaons' PT distribution is expected to be peaked at larger values.

The signal and background distributions for these variables are shown in Figure 3.1

Note that the variables relative to the re-fit cannot be used in this phase, because they are obtained by fixing some parameters (e.g. the B mass in the most constrained case), and are therefore fully correlated with these latter. Set I only is used.
The correlation matrices for the selected variables in the signal and background case are shown in Figure 3.2. Those matrices also include a seventh variable: the transverse momentum of the J/ψ, which is highly correlated with the B transverse momentum, and, for this reason, although initially taken into account, has not been included in the MVA training. Regarding the six selected variables, the transverse momenta are partially correlated, while the other quantities show negligible correlations for the signal sample, and minor correlations for the background sample.
However, the variables are linearly decorrelated before the beginning of the training, diagonalizing the correlation matrix and creating another set of variables with no true physical meaning, but with the same per event method response.

The performance of the MVA is then computed on a different MC sample, independent with respect to the one used for the training phase. Figure 3.3 shows the Receiver Operating Characteristic (ROC) curve, representing the performance in the plane $\epsilon - r$ where r is the background rejection (1 - background efficiency) and ϵ is the signal efficiency. This curve is drawn for three different MVA methods (Fisher discriminants, Boosted Decision Tree and Likelihood). Since the performance are very similar, the Likelihood method was chosen for the reasons discussed above. In Figure 3.5 the distribution of the MVA output variable for both signal and background is shown.

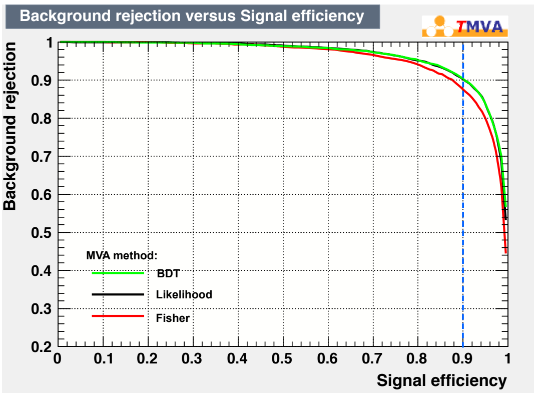

Figure 3.3: MVA methods performance (ROC curve). The blue dashed line shows the efficiency corresponding to the applied cut, determined from the plot on the right.

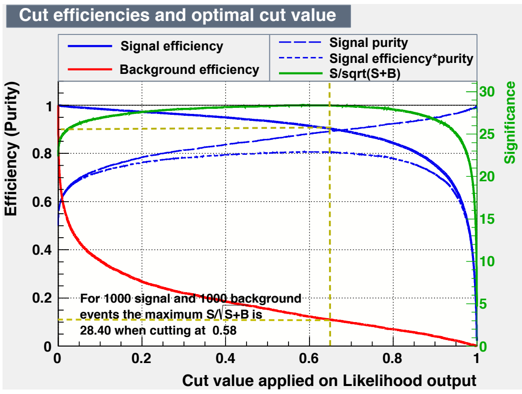

Figure 3.4: Performance of the PLE method in the MVA. The yellow dashed lines show the applied cut with the corresponding efficiency on signal and background.

In Figure 3.4 are the performance of the PLE method in more detail, showing also the efficiency for signal and background, the signal purity and the significance as a function of the cut.

3.3.2 Classification

Once the training information is extracted from signal and background samples and stored into the weights file, the multivariate analysis is ready to be applied to the preselected dataset. For each event i, $r_{\mathcal{L}}$ is computed according to Equation (3.3.3), using the PDFs from the training phase.
The cut to be applied has been set to $r_{\mathcal{L}} > 0.65$ by observing the behaviour of the curves in Figures 3.4 and 3.5. The chosen cut corresponds to an efficiency of about 90% on the signal and $\sim$ 11% on the background.
The B mass distribution in data before and after this cut is shown in Figure 3.6 for two different kind of variables: those with the J/ψ mass constraint only (set I), and those with the Primary Vertex Pointing and the π^0 and J/ψ mass constraint (set II).

3.4 Analysis of Monte Carlo events

The observation of the MC simulation plays a central role in every particle physics analysis. It allows to study the characteristics of the signal, helping to interpret correctly the results on real data.
The decay $B \to J/\psi\ \omega\ K$ has been generated following the phase space model, according to which each B meson decays in three daughters without any intermediate resonance.
A set of acceptance and kinematic cuts is applied at generator level to produce only

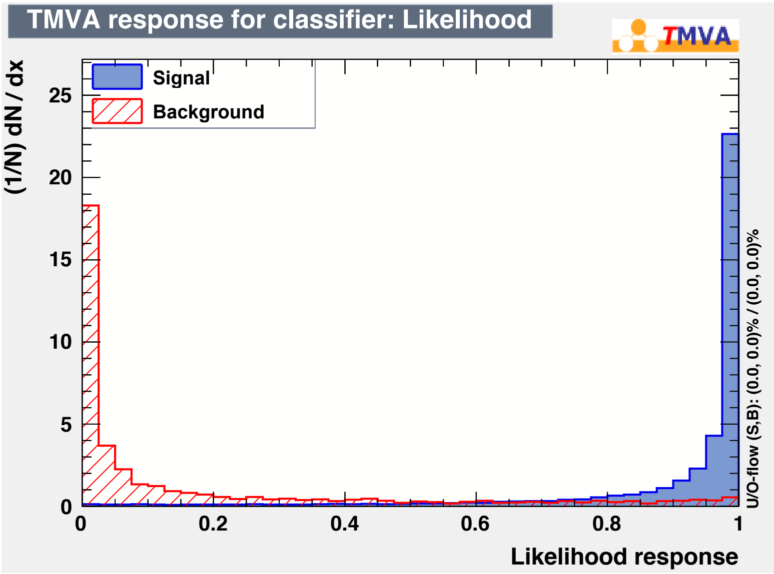

Figure 3.5: MVA PLE method response for signal and bacground.

events that could be triggered and reconstructed by the on-line software, in order to match the real case scenario and speed up the computational process. The simulated dataset is then processed in order to introduce the detector effects with the GEANT4 package.
Figure 3.7 shows the $J/\psi\ \omega$ invariant mass (computed from the *true* momenta) distribution before and after the reconstruction and selection cuts. The non reconstructed spectrum shows a tail for masses smaller than the threshold value: it is due to the ω mass spectrum, which is generated with asymmetric tails, as can be seen in Figure 3.8.

In this section the expected B mass distribution is shown for the different re-fit configurations, after the preselection has been performed, and some resolution studies are presented.

3.4.1 Lineshapes

In order to study the effects of the decay chain re-fit and to understand what should be expected from real data, the B mass distribution for the signal MC is shown in Figure 3.9 for the re-fit configurations I and II.
Set II shows a narrower peak with respect to set I, as expected after having constrained the π^0 mass and the vector pointing.

An attempt to fit the B mass distribution on the signal MC shows that its tails are sizeable, hence it can't be described by a single gaussian function, in both I and II re-fitted variables. A better description is provided by the sum of two gaussian functions

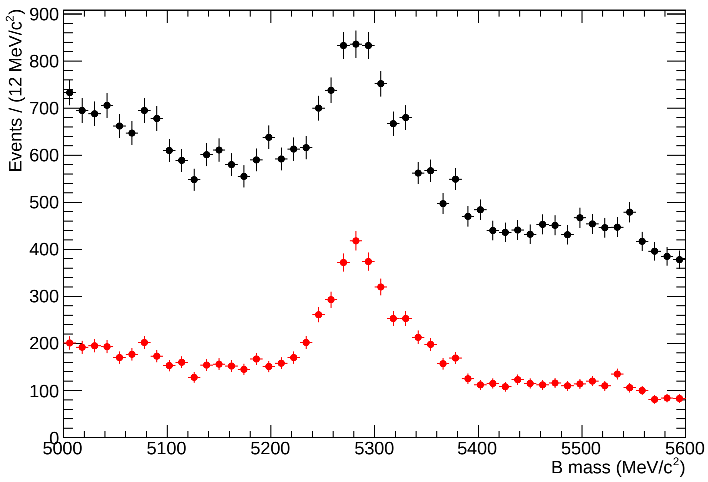

(a) set I.

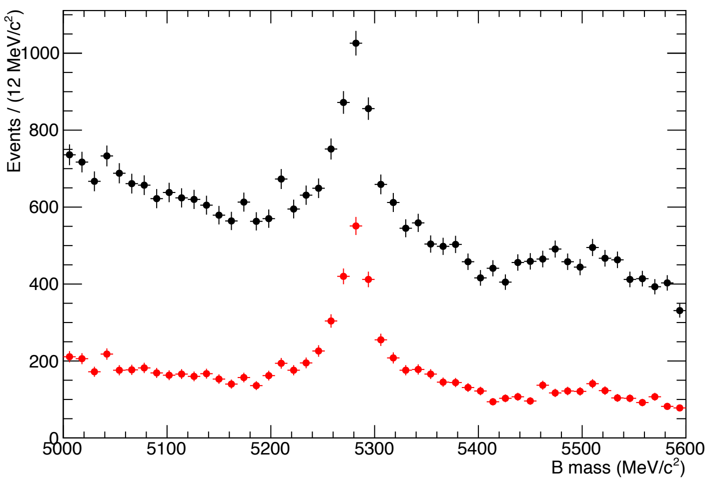

(b) set II.

Figure 3.6: B mass distributions before (black dots) and after (red dots) the cut on $r_{\mathcal{L}}$.

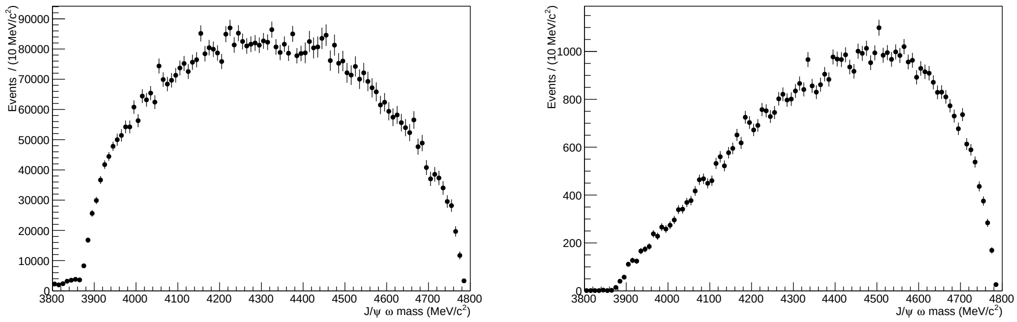

Figure 3.7: $J/\psi\ \omega$ *true* invariant mass before the reconstruction (left) and after the preselection cuts (rigth).

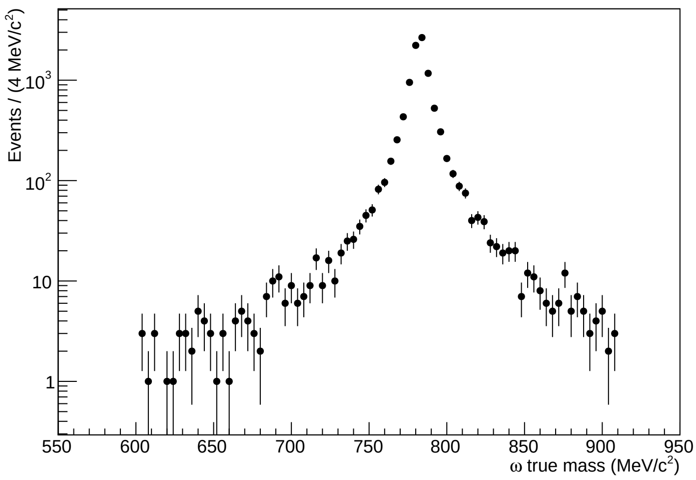

Figure 3.8: Semi-logarithmic scale plot of $M(\omega)$ for the control MC sample.

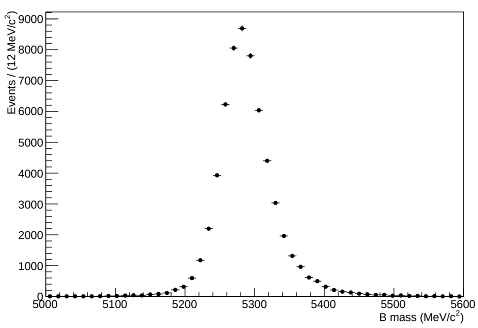

(a) set I.

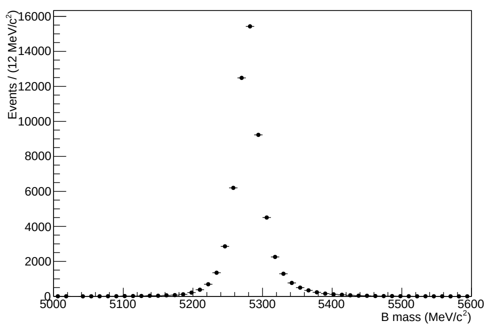

(b) set II.

Figure 3.9: B mass distributions on signal MC.

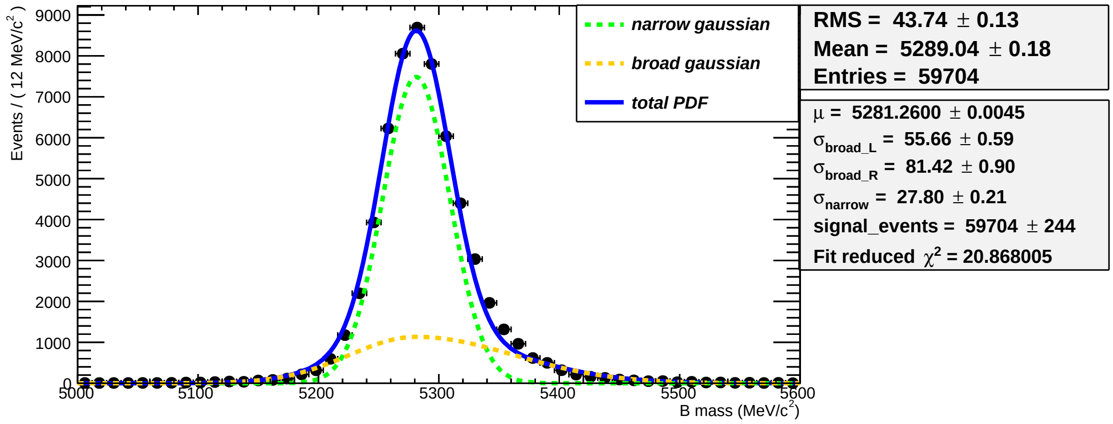

(a) Set I.

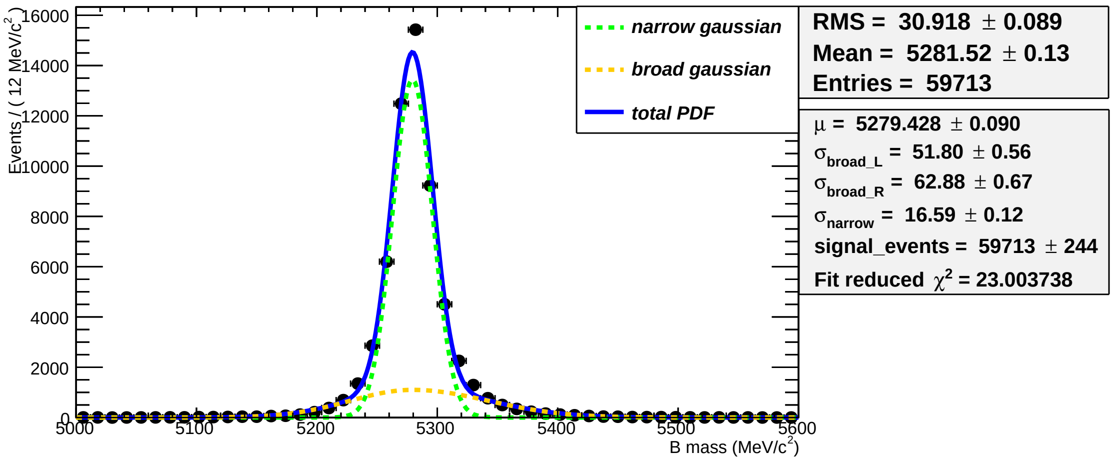

(b) Set II.

Figure 3.10: Gaussian fits on mass distributions on signal MC.

with the same mean but different standard deviations: a broad one to reproduce the tails and a narrow one for the peak. Furthermore, the tails are not symmetric, thus a bifurcated gaussian is chosen for the broad contribution, as shown in Figure 3.10. The χ^2 of these fit is far from being acceptable. This is due to the imprecision of the model with respect to the statistical level of the distribution. However, the goal here is only to extract from MC a rough idea of the shape of the B mass spectrum in order to use a similar description on real data.

Figure 3.11 shows the distributions of ω and π^0 masses for different re-fit configurations. Being fixed to its nominal value in sets II and III, the neutral pion mass is

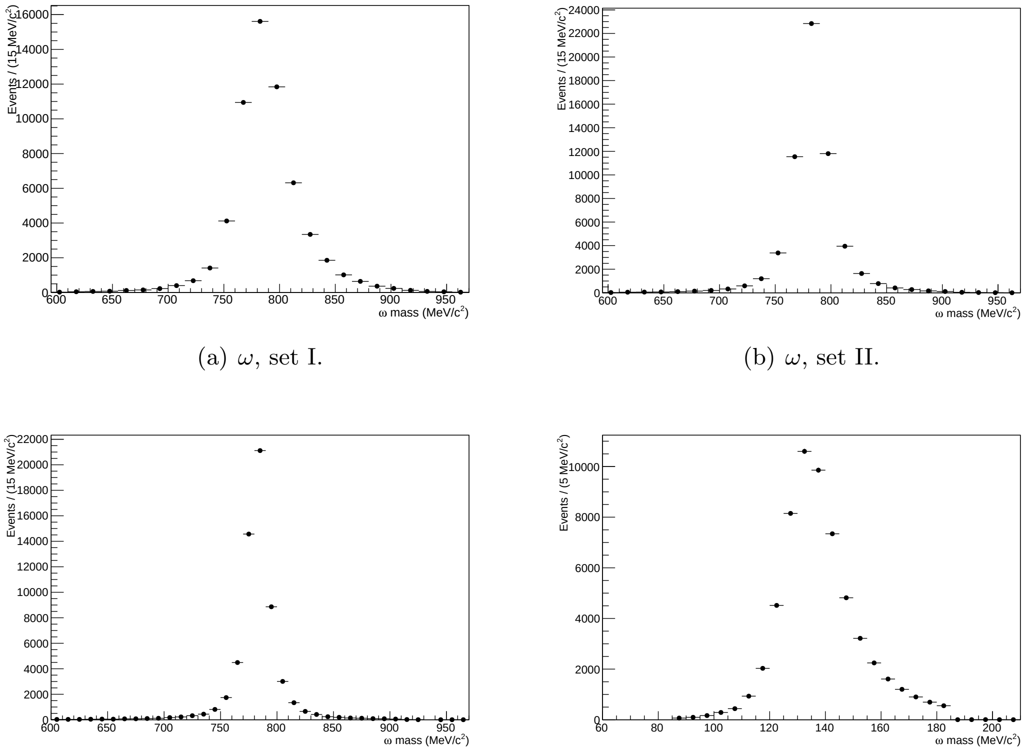

(a) ω, set I.

(b) ω, set II.

(c) ω, set III.

(d) π^0, set I.

Figure 3.11: ω and π^0 mass distributions on signal MC.

only shown for set I. Its right tail is more populated than the left one, resulting in an asymmetric distribution. This effect is well known and it is attributed to the non perfect treatment of the cases where the clusters associated to the two photons are overlapped in space and the energy release in the calorimeter cells which are in common is not properly taken into account, resulting in a sort of double counting. A new reconstruction software which partially cures this problem is under development by the calorimeter group. It seems reasonable to infer that the asymmetry on the π^0 mass spectrum is the reason for the asymmetry of the B mass spectrum.

3.4.2 Mass resolutions

In order to choose an appropriate binning for the study of the $J/\psi\ \omega$ invariant mass distribution, the resolution on this variable in the present analysis can be estimated from MC. Furthermore, the X(3872) and the $\chi_{c0}(2P)$ masses are very close, thus the $J/\psi\ \omega$ mass resolution determines whether or not the two peaks can be resolved.
In particular, $M(X(3872)) = 3871.68 \pm 0.17\ MeV/c^2$ and $M(\chi_{c0}) = 3918.4 \pm 1.9\ MeV/c^2$),

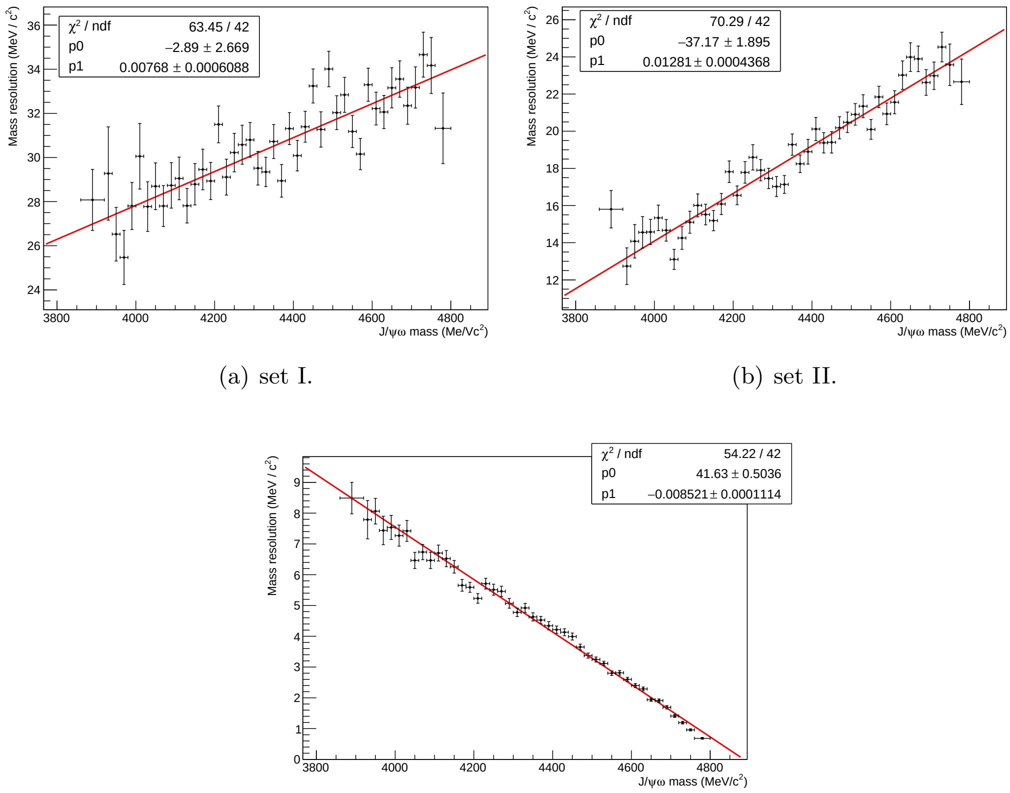

(a) set I. (b) set II.

(c) set III.

Figure 3.12: $J/\psi\ \omega$ mass resolution (gaussian fit method).

thus:

$$\Delta M = M(X(3872)) - M(\chi_{c0}) = 47.0 \pm 1.9\ MeV/c^2. \tag{3.4.1}$$

Calling σ the mass resolution, a reasonable expectation is that the two peaks can be well distinguished if the distance between their mean values is more than 4σ. In this case, the worst resolution that would allow to resolve the two peaks is $\sigma_{max} \approx 12\ MeV/c^2$.

The resolution has been computed from the MC sample after the application of the MVA cut. The quantity

$$\delta M = M_{reco}(J/\psi\omega) - M_{true}(J/\psi\omega) \tag{3.4.2}$$

is defined for each bin of the M_{true}, the MC truth $J/\psi\ \omega$ mass. M_{reco} is the same quantity, reconstructed in an identical way as real data.
These δM distributions have been fitted with a gaussian function, whose standard deviation represents the mass resolution that we want to measure.

The current MC sample contains few events in the low mass region; this affects the accuracy of the above described procedure. In order to compensate this lack of statistic, the bin width in the M_{true} variable, initially set to 40 MeV, is increased by merging adjacent bins until the resulting bin contains a minimum of 150 events.
The result is shown in Figure 3.12: the points correspond to the standard deviations of the fitted gaussians.
The behaviour of the points suggests a linear fit of these data; the low χ^2 obtained from the fit shows that it well describes the resolution function. The slope of the re-fit configuration III has opposite sign with respect to the other two. This can be explained as an effect of the re-fit itself: while in the *free* B mass cases the absolute fluctuations on particles' momenta are expected to become larger when these momenta increase, in case III, the resolution has a negative slope because the higher the $J/\psi\,\omega$ system mass, the more the B system mass is close to it (the kaon is soft) and in this refit scheme the B mass is fixed to its nominal value, i.e. it has $\sigma = 0$.
Anyway, despite the different slope of the resolution functions, it appears clear that set III provides more precise results, as expected, at low masses.

However, the method for the resolution measurement can be improved in our case: in fact δM is not always well described by a gaussian function. This distribution is shown for three different M_{true} intervals in Figure 3.13: it is clear that its sizable tails, evident in particular in cases I and II, prevent accurate results from the fit.

A different approach has therefore been used: generalizing the properties of a normal distribution to the distribution observed on MC, the resolution σ has been measured as the value which satisfies:

$$\frac{\int_{\mu-\sigma}^{\mu+\sigma} \mathcal{M}(J/\psi\,\omega)dm}{\int_{-\infty}^{+\infty} \mathcal{M}(J/\psi\,\omega)dm} \simeq 0.6827 \tag{3.4.3}$$

where m is the mass variable, $\mathcal{M}(J/\psi\,\omega)$ is the observed distribution on MC, and μ its mean. The integral of each histogram is thus recursively calculated in symmetric intervals centered in μ, increasing each time the integration interval by two times the bin width. This latter is also taken as the error on σ. The results of this approach are shown in Figure 3.14

In this case the resolutions for sets I and II result slightly worse. This is not surprising, considering the fact that the gaussian fit underestimates the tails of the real distributions. Set III, instead, gives more stable results.
The values obtained from the linear fits is Figure 3.14 will be used hereinafter to evaluate the expected $J/\psi\,\omega$ mass resolution for a given mass value. According to this fit, $\sigma(M(J/\psi\,\omega) = M(X(3872)) \approx 8.45$, thus the two peaks should be resolved.

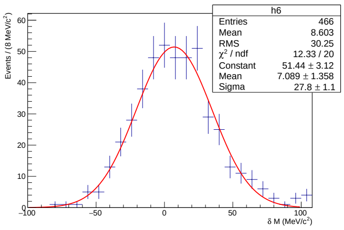

(b) a

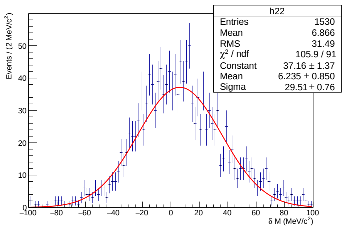

(c) b

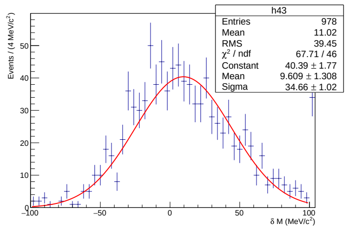

(d) c

(d) set I

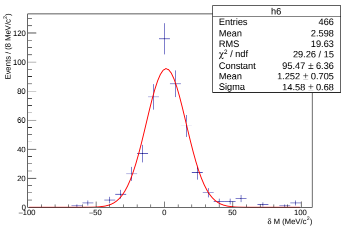

(f)

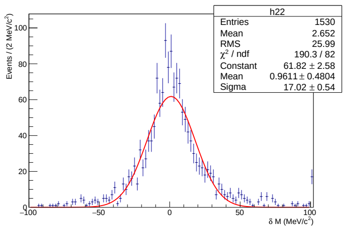

(g)

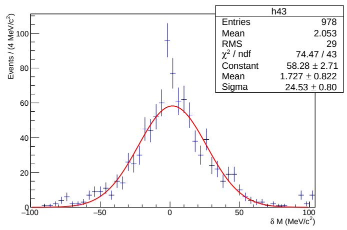

(h)

(h) set II

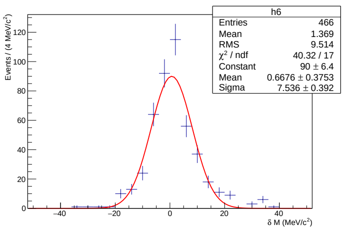

(j)

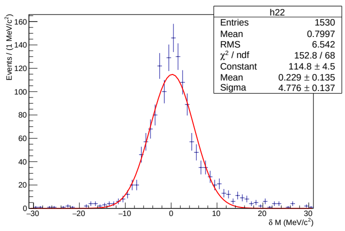

(k)

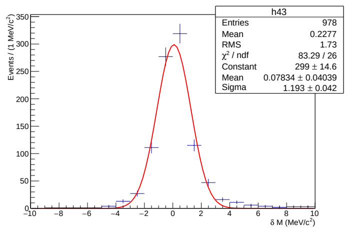

(l)

(l) set III

Figure 3.13: δM distributions for the three re-fit configurations corresponding to three different intervals of $M_{true}(J/\psi\omega)$: [3980, 4000] MeV/c^2 (a), [4300, 4320] MeV/c^2 (b), [4720, 4740] MeV/c^2 (c).

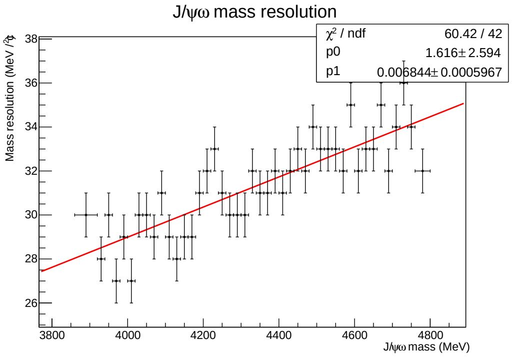

(a) set I.

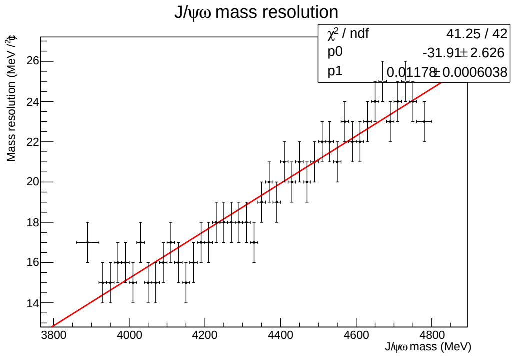

(b) set II.

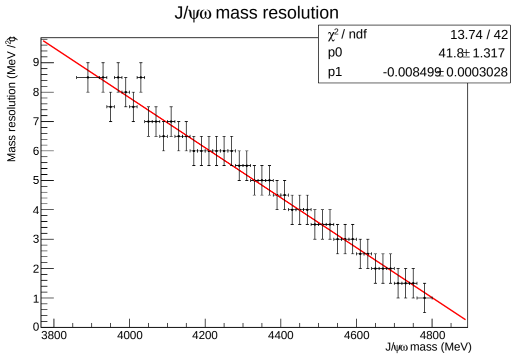

(c) set III.

Figure 3.14: $J/\psi\ \omega$ mass resolution (integral evaluation method).

The quantity $M_{reco} - M_{true}$ is also shown for the ω and the π^0 in Figure 3.15. In this case, besides presenting sizable tails, the distributions are not even symmetric. They are therefore fitted with a broad bifurcated gaussian distribution plus a narrower, symmetric peak with the same mean. It is clearly visible how the re-fit procedure improves the ω resolution: the distribution becomes significantly narrower and more symmetric in set III with respect to set II and especially to set I.
Nevertheless, in any case the experimental resolution results larger than the ω intrinsic width ($8.49 \pm 0.08\ MeV/c^2$, PDG value.)
In the case of the neutral pion, only the re-fit case I is, of course, shown, being its mass constrained in case II and III.

3.5 B mass fit and background subtraction

In order to obtain the signal distributions of data, a fit is performed on the $B^{\pm}$ mass distribution after the MVA cut, describing the signal and the background components.

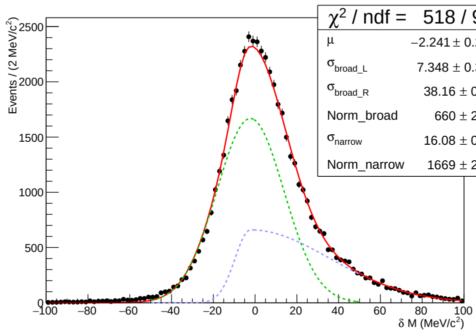

(a) ω, set I.

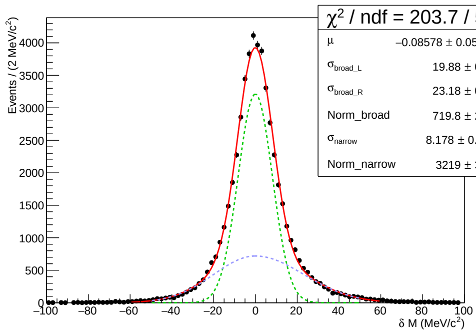

(b) ω, set II.

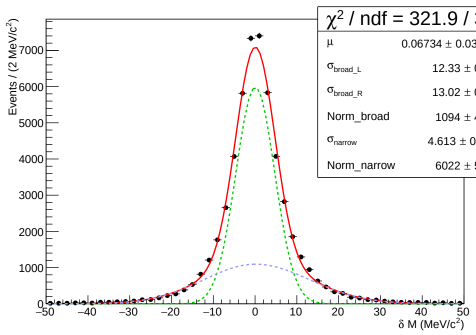

(c) ω, set III.

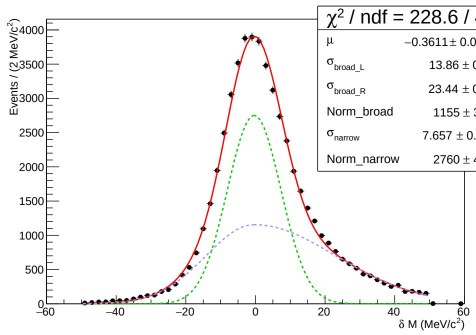

(d) π^0, set I.

Figure 3.15: $J/\psi\ \omega$ mass resolution for sets I and II. The narrow (dashed green) and broad (dashed blue) components of the fit distribution are shown along with the total PDF (solid red). The parameters Norm_broad and Norm_narrow indicate the height of the two peaks.

This allows to perform a background subtraction with the so-called ${}_s\mathcal{P}lot$ technique. This technique is a background subtraction tool, described in detail in Appendix A. Restricting the field to the specific case of this analysis, it can be summarized as follows: given a dataset consisting of two different sources, namely signal and background, merged together, whose PDFs for each source are known for a certain discriminating variable, to each event a set of weights (*sWeights*) can be assigned, proportional to the likeliness that the event belongs to each of the sources. This allows to build histograms for the isolated contribution of one of the sources. The discriminating variable used in this case is the $B^{\pm}$ mass for the signal peak.
This procedure is performed using the RooFit toolkit [57], provided by the ROOT framework.

3.5.1 Mass fit

Unbinned extended likelihood fits performed on data for configurations I and II are shown in Figure 3.16. A decreasing exponential PDF has been added to the double-gaussian

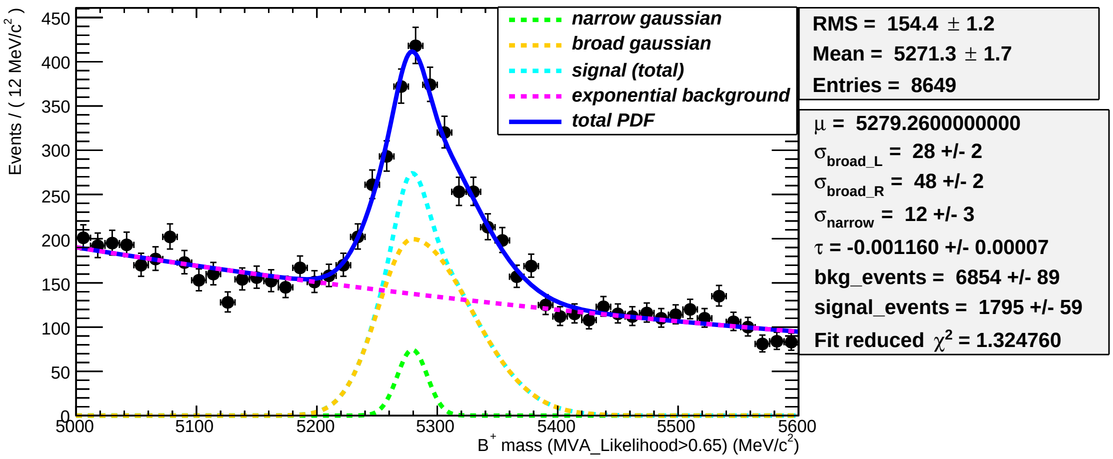

(a) set I.

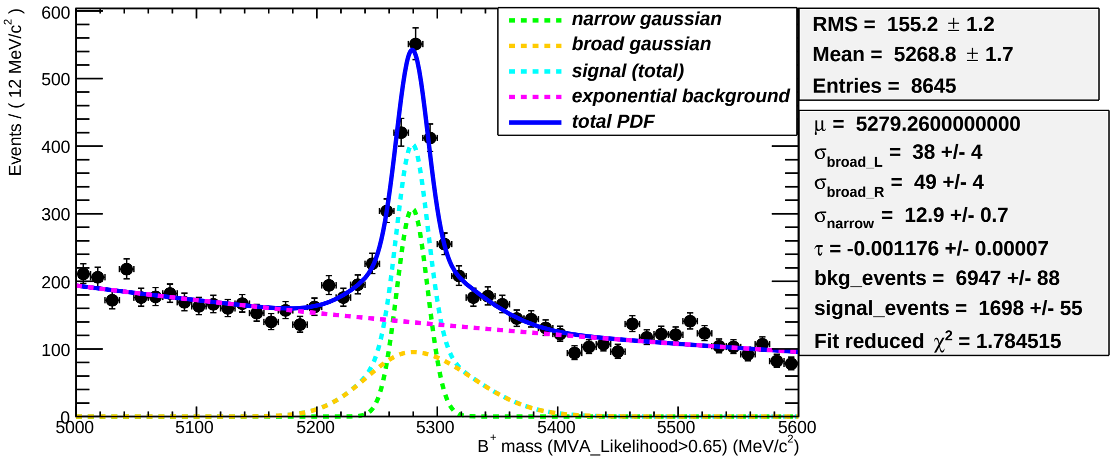

(b) set II.

Figure 3.16: Fits of B mass distributions on data.

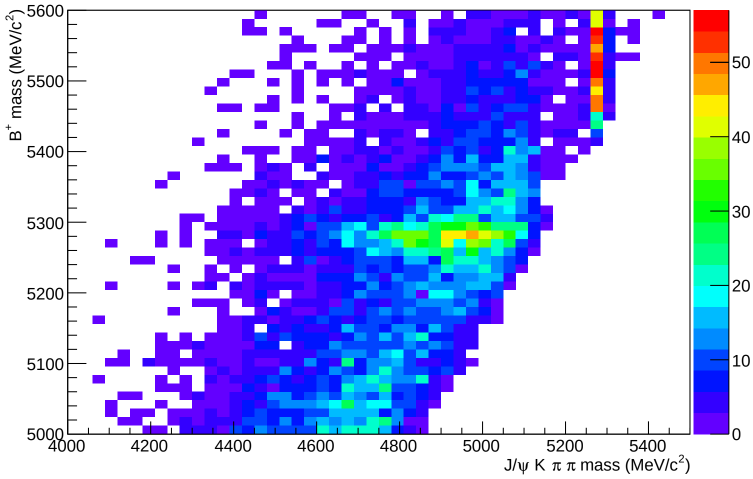

Figure 3.17: $J/\psi\ \pi^+\pi^-\ K$ vs $J/\psi\ \omega\ K$ dalitz plot.

signal, previously tested on MC, in order to describe the background distribution. The total pdf, thus, can be expressed as:

$$f_{tot} = N_{bkg} \cdot e^{\tau \cdot M} + N_{sig} \cdot (N_1 \cdot G_{narrow}(M; \mu, \sigma_{narrow}) + N_2 \cdot G_{broad}(M; \mu, \sigma_{broad_L}, \sigma_{broad_R})) \tag{3.5.1}$$

where M is the mass variable, N_{bkg} and N_{sig} are respectively the background and signal yields, G_{narrow} and G_{broad} are the two gaussians, and N_1 and N_2 are their respective normalizations. σ_{broad_L} and σ_{broad_R} indicate the left and right standard deviations of the bifurcated gaussian.
The mean of the gaussians is constrained in the fit to the B mass nominal value.

Although the ratios between the different components are quite different in the two re-fit configurations, the number of signal events is consistent, as it should be in the case of a correct re-fit procedure and PDF modelling. The large asymmetry of the B mass in set I is probably due to the π^0 mass shape on data which will be shown in the next section.

An excess is visible around $M(B) = 5500\ MeV/c^2$. The observation of the scatter plot in Figure 3.17 clearly shows that this is caused by the decay $B \to J/\psi\ \pi^+\pi^-\ K$. This contribution could be eliminated by cutting the $J/\psi\ \pi^+\pi^-\ K$ at $\sim 5200\ MeV/c^2$. Anyway this would also reject a significant amount of other events in the high B mass region, making more critical the determination of the background shape, which would not be anymore successfully represented by a simple decrasing exponential. We therefore decided not to apply this cut. Furthermore, this excess seems to be not big enough and far away from the B mass region to strongly affect the result of the fit.

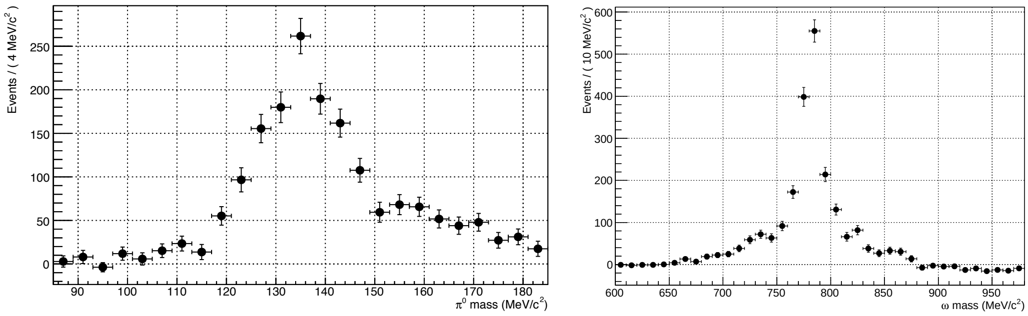

Figure 3.18: Background-subtracted π^0 (left) and ω (right) mass distributions.

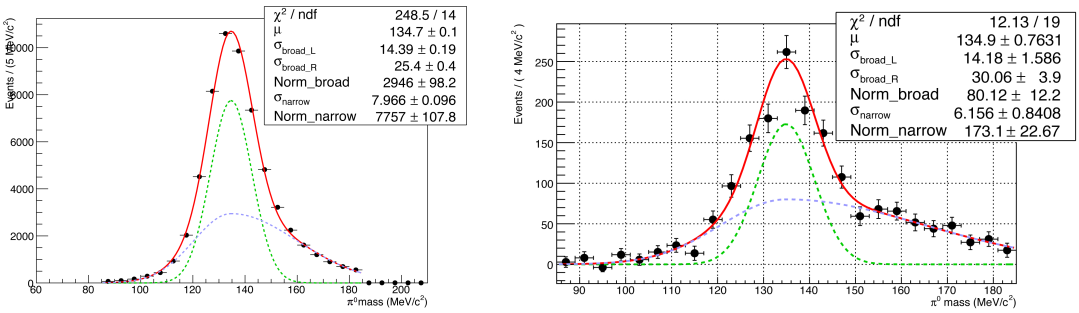

Figure 3.19: Signal π^0 mass distribution on MC (left) and on data (right). The narrow (dashed green) and broad (dashed blue) components of the fit distribution are shown along with the total PDF (solid red). The parameters Norm_broad and Norm_narrow indicate the height of the two peaks.

3.5.2 Background subtraction: ${}_s\mathcal{P}lot$

It appears clear from the fits that the B signal is significantly sharper in the re-fit II case. This variable will be used hereinafter for the fit of the B mass, but all the other sets will be kept in order to be able to choose the best set for every observable and every operation.

The application of the ${}_s\mathcal{P}lot$ technique to the B mass distribution allows, at this point, to obtain the background-subtracted (i.e. weighted) distributions of the variables of interest.
Figure 3.18 shows the weighted π^0 and ω masses. The former exhibits the same asymmetry observed on MC, but this effect is much stronger here. A comparison is made in Figure 3.19: a fit with a narrow, symmetric gaussian plus a broad asymmetric one is shown for MC and data; it is evident that the broad component is more populated on data.
The correct reproduction of these distributions is a further hint that the PDFs used for the B fit are fairly accurate. For the ω distribution, variables from set III are used.

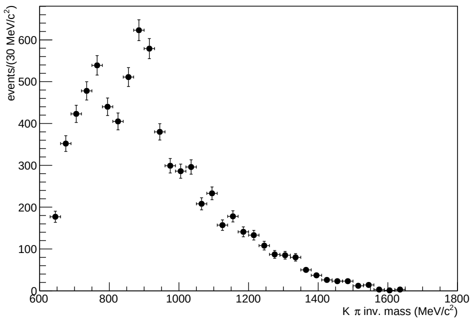

(a) $K\ \pi$ before sPlot

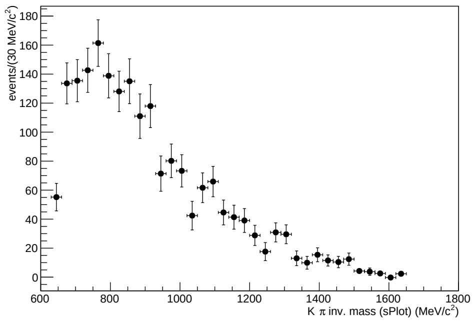

(b) $K\ \pi$ after sPlot

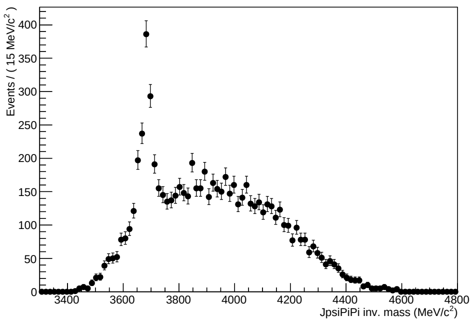

(c) $J/\psi\ \pi^+\ \pi^-$ before sPlot

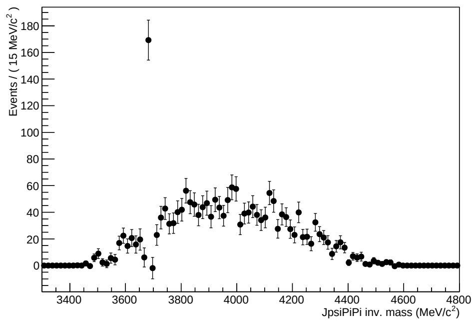

(d) $J/\psi\ \pi^+\ \pi^-$ after sPlot

Figure 3.20: $K\ \pi$ and $J/\psi\ \pi^+\ \pi^-$ spectra before and after the background subtraction.

3.5.3 Known resonances subtraction

Before proceeding to the examination of the $J/\psi\ \omega$ invariant mass, it is important to remove from the data sample all the known unwanted contributions. The presence of resonant states in the decay chain could indeed reflect into the final observed spectrum. The most likely states that could be present in our sample are the $\psi(2S)$ and $K^*(892)$ mesons since there are many B decays with these resonances as daughter particles. Moreover:

- $K^*(892)$ decays to $K\ \pi$ almost 100% of the times;
- $\psi(2S)$ decays to $J/\psi\ \pi^+\ \pi^-$ about 34% of the times;

Figure 3.20 shows the $K\ \pi$ and $J/\psi\ \pi^+\ \pi^-$ mass spectra before and after the background subtraction.

The $\psi(2S)$ peak stands out clearly over the phase space shape before the ${}_s\mathcal{P}lot$, and is not completely removed after it. The region $3650\ MeV/c^2 < M(J/\psi\ \pi^+\ \pi^-) < 3725\ MeV/c^2$ is therefore cut out before building the $J/\psi\ \omega$ histogram. These cut values have been determined from the plot before the ${}_s\mathcal{P}lot$ application.

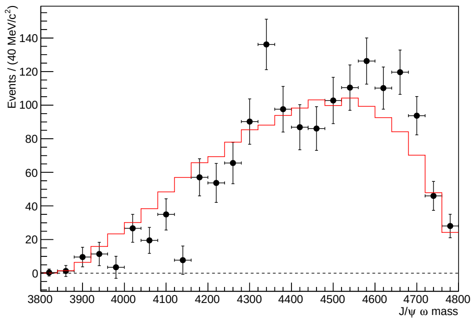

(a) set I

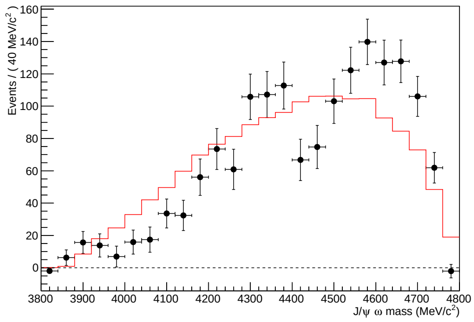

(b) set II

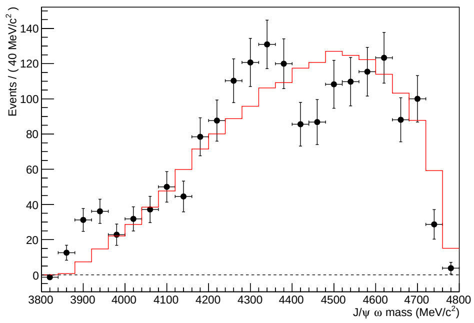

(c) set III

Figure 3.21: $J/\psi\ \omega$ invariant mass distribution on data (dots) and MC (red line) for the three decay chain re-fit schemes.

On the other hand, the $K^*(892)$ contribution seems to be appropriately rejected, as it does not appear in the isolated signal distribution; for this reason, no further rejection cuts are applied.

3.6 $J/\psi\ \omega$ invariant mass spectrum

The resulting $M(J/\psi\ \omega)$ invariant mass distribution on data is shown in Figure 3.21, along with the corresponding MC distribution, normalized to the same integral and having submitted the MC events to exactly the same treatment as real data.

In all the three refit configurations the agreement with MC is not satisfactory. They all show a structure with three bumps: one near threshold, one around 4350 MeV/c^2 and another at $\sim 4600\ MeV/c^2$.

Some checks have been carried out in order to try to understand these structures. In Figure 3.23 the scatter plot $M(K\omega, J/\psi\omega)$ is shown. An accumulation of events is visible right at $M(J/\psi\omega) \simeq 4600\ MeV/c^2$ and $M(K\omega) \simeq 1300\ MeV/c^2$. This is interpreted as

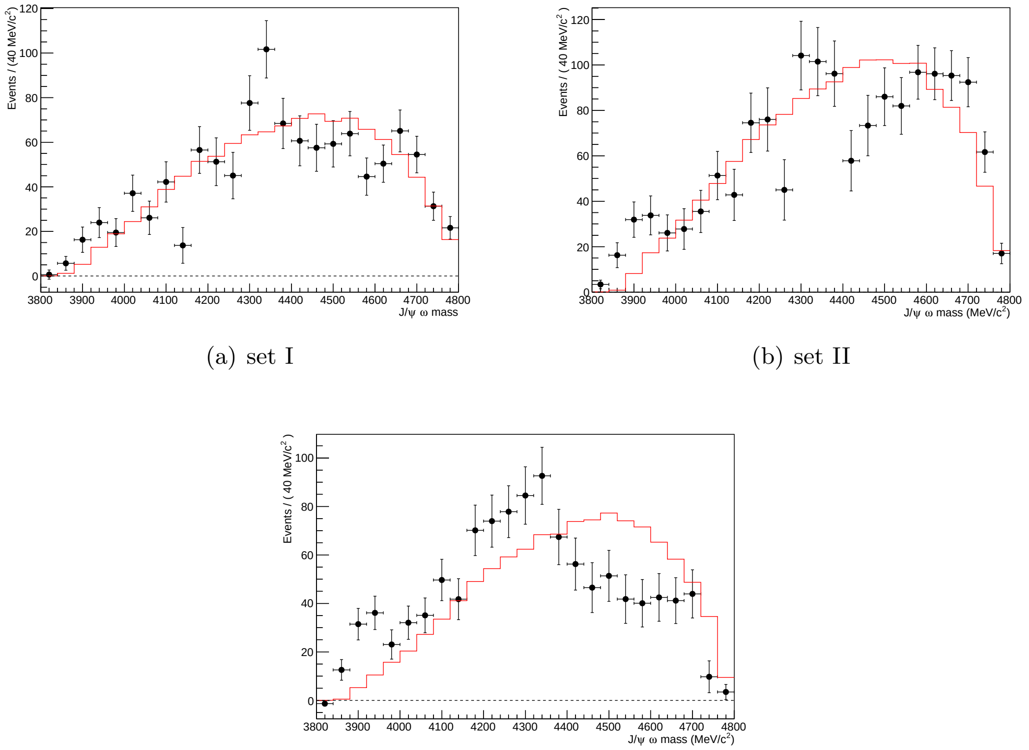

(a) set I

(b) set II

(c) set III

Figure 3.22: $J/\psi\ \omega$ invariant mass distribution on data (dots) and MC (red line) after removal of the K(1270) contribution.

coming from the decay chain

$$\begin{aligned} &B^+ \to J/\psi\ K(1270); \\ &K^+(1270) \to K^+\ \omega \end{aligned} \tag{3.6.1}$$

The relatively large contribution of this decay is in fact corroborated by the values of the branching ratios reported in the PDG:

$$BR(B^+ \to J/\psi\ K^+(1270)) \times BR(K^+(1270) \to K^+\ \omega) \approx 2 \times 10^{-5} \tag{3.6.2}$$

to be compared to:

$$BR(B^+ \to X(3872)\ K^+) \times BR(X(3872) \to J/\psi\ \omega) \approx 6 \times 10^{-6} \tag{3.6.3}$$

and:

$$BR(B^+ \to K^+\ J/\psi\ \omega) \approx 3 \times 10^{-4} \tag{3.6.4}$$

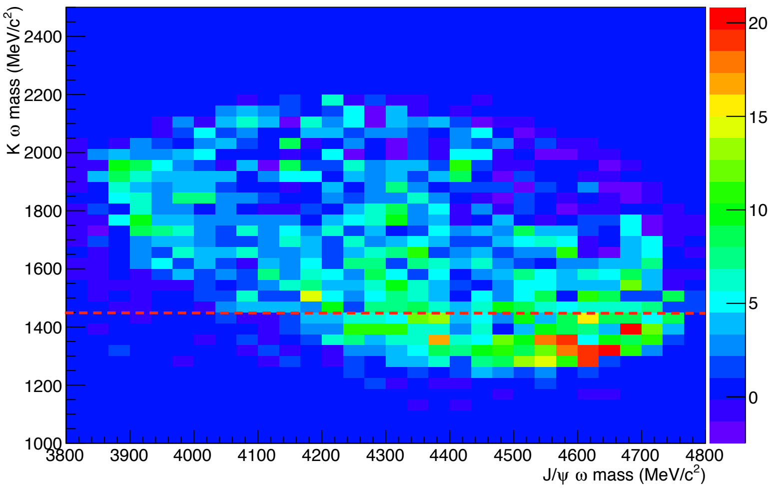

Figure 3.23: $J/\psi\ \omega$ vs $K\ \omega$ scatter plot. The red dashed line shows the applied cut.

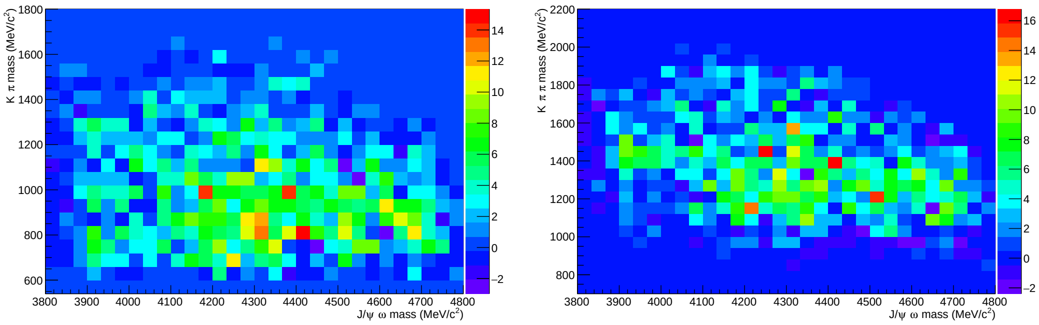

Figure 3.24: $M(J/\psi\ \omega)$ vs $M(K\ \pi)$ (left) and $M(J/\psi\ \omega)$ vs $M(K\ \pi\pi)$ (right) scatter plots.

In order to remove it, a lower cut at 1450 MeV/c^2 is applied on the $K\ \omega$ invariant mass. This value has been determined summing the $K(1270)$ mass to 4 times its nominal half-width ($\Gamma(K(1270)) = 90 \pm 20 MeV$). The experimental resolution has not been considered, being much smaller than the intrinsic width.

Although it implies a significant loss of statistic, this cut seems to remove the excess around 4600 MeV/c^2. Nevertheless, the agreement between data and MC is still not good. Figure 3.22 shows the obtained distributions. The excess around 4300 MeV/c^2 is still clearly visible, particularly for the re-fit I.

Aiming at identifying the source of this effect, the invariant mass spectra of various combination of the particles present in the analyzed final state have been observed, in Figure 3.24 the scatter plots of $M(J/\psi\ \omega)$ vs $M(K\ \pi)$ and $M(J/\psi\ \omega)$ vs $M(K\ \pi\pi)$ are shown. No particular accumulation is visible around 4300 MeV/c^2.

Since at the moment we are not able to describe the spectrum behaviour in the full range, the analysis of the $J/\psi\ \omega$ spectrum has been therefore limited to the low mass region. The cut is applied on the distribution of set I, being this the less biased variable available. Nevertheless, the results will still be observed on set III, because, as shown in Section 3.4.2, it provides the best mass resolution.

3.7 Efficiency correction

Every selection step, ideally performed to reject background events only, inevitably implies a loss of signal. These efficiency losses occurring as a concequence of the different steps of the selection chain must be taken into account in order to correctly extract the physical quantities we are interested in.
The correction to be applied will be, in principle, not constant with respect to the $J/\psi\ \omega$ invariant mass and needs thus to be evaluated bin-by-bin as the ratio between the number of signal events before and after the full analysis chain.
In particular, the denominator of this ratio is the histogram of the *true* $J/\psi\ \omega$ invariant mass in the *control* MC sample, simulated with the EvtGen generator, where the only requirement which has been imposed is that all the B daughter particles are within the LHCb geometrical acceptance. The efficiency of the acceptance, in fact, is not considered here since we are not interested in absolute measurements.
The numerator of the efficiency, on the other hand, is the same histogram of the *true* $J/\psi\ \omega$ invariant mass, limited to those events surviving the full analysis chain which is obviously applied to the *reconstructed* quantities (with the exception of the first step discussed hereinafter).

The main steps which have been considered for the efficiency calculation can be summarized as follows:

1. **Trigger and stripping cuts**: the effect induced by the trigger and by the stripping procedure is taken into account by applying suitable cuts at generator level. These cuts are very conservative: they only reject events which have no chances to be neither triggered nor reconstructed. This also entails a significant decrease of the computing time needed to simulate the detector response with GEANT4, by limiting this operation to the interesting events.

2. **Reconstruction**: this step includes the efficiency of track reconstruction, particle identification and B candidate reconstruction. The loss of events occurring during the re-fit procedure is also taken into account here.

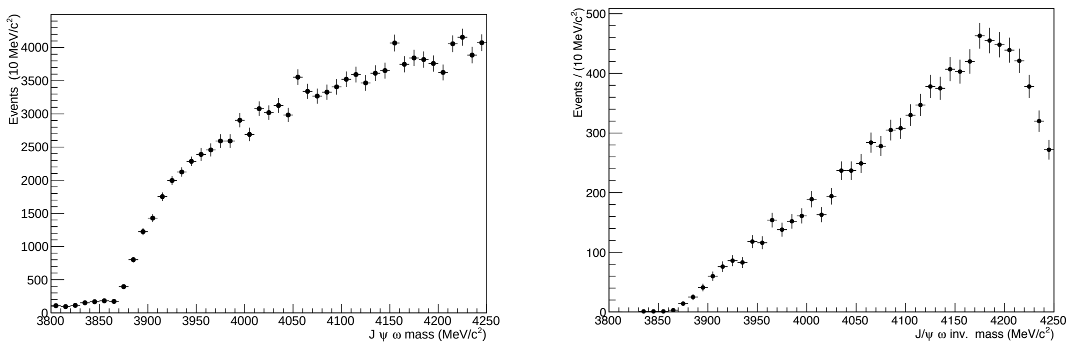

(a) The MC control sample (left) and the analysis sample after all the cuts (right).

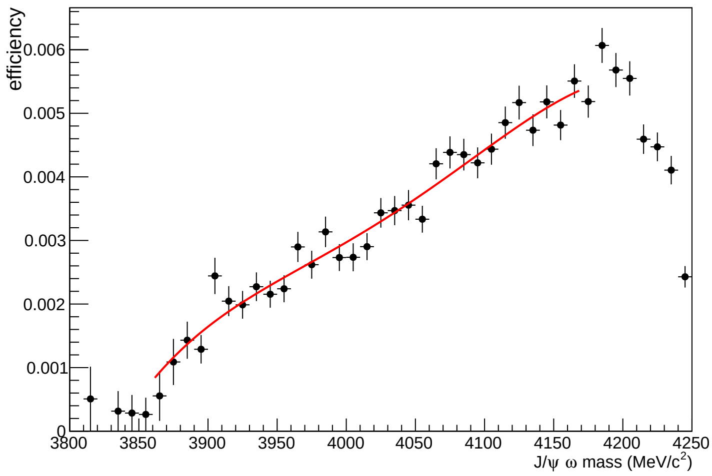

(b) Selection efficiency after all the analysis cuts.

Figure 3.25: MC distributions and efficiency for steps 1-7.

3. **Preselection**: this step corresponds to the application of the cuts described in Table 3.4 and discussed in Section 3.2.4.

4. **MVA**: here the efficiency losses due to the multivariate analysis cut is considered.

5. $\boldsymbol{\psi}$**(2S) resonance subtraction**: the removal of the contribution from this particle obviously affects the efficiency, thus it must be taken into account.

6. **K(1270) resonance subtraction**: the analysis required the application of an additional cut aiming at removing this resonance's contribution.

7. $\mathbf{J}/\boldsymbol{\psi\omega}$ **invariant mass cut**: this step concerns the effect of the cut announced at the end of Section 3.6 and discussed in detail in Section 3.9, where the analysis will be restricted to the range 3800 $MeV/c^2 \ < \ M(J/\psi\ \omega) \ < \ 4250\ MeV/c^2$.

In Figure 3.25(a) the MC $J/\psi\ \omega$ mass distribution before and after performing all these operations is shown.

The total efficiency is therefore expressed as:

$$\epsilon(M_{J/\psi\omega})_{1-7} = \frac{N_{steps\ 1-7}}{N_{in\ acceptance}} \tag{3.7.1}$$

Figure 3.25(b) shows the overall efficiency on signal MC events. A 4^{th} degree polynomial is fitted on this distribution in order to obtain an analytical form as accurate as possible. The fit range is limited to $M(J/\psi\ \omega) > 3870\ MeV/c^2$, because for lower masses the MC events are too few to accurately compute the efficiency (note that the kinematic threshold is $M(J/\psi) + M(\omega) = 3882.6 MeV/c^2$). The efficiency function thus obtained is however used to correct also events with lower invariant masses: in fact it is extrapolated down to a mass of 3860 MeV/c^2.

It must be stressed that the accuracy of this operation is crucial for the final result: in fact, the efficiency drops rapidly in the near threshold region, where the $X(3827)$ and $\chi_{c0}(2P)$ are expected, thus the correction applied on data amplifies the number of events by a factor which varies largely from bin to bin.
Inaccuracies in the efficiency measurements would therefore reflect in an under- or overestimation of the number of events in the region of interest with respect to the rest of the spectrum.
A new MC production has been submitted in order to enrich the sample in the low mass region $M(J/\psi\ \omega) < 4200\ MeV/c^2$. Unfortunately, it is not yet available for the analysis.

In the following section the observed $J/\psi\ \omega$ spectrum will be compared with BaBar's results. For this aim, the knowledge of the efficiency limited to steps 1-4 is needed:

$$\epsilon(M_{J/\psi\omega})_{1-4} = \frac{N_{steps\ 1-4}}{N_{in\ acceptance}} \tag{3.7.2}$$

Figure 3.26(a) shows the MC $J/\psi\ \omega$ mass distribution before and after performing the operations 1-4. The resulting efficiency ϵ_{1-4} is shown in Figure 3.26(b)

3.8 Comparison with BaBar results

Before continuing the analysis, in this section a comparison of our data with BaBar's is made.
As above mentioned the $J/\psi\ \omega$ invariant mass spectrum that we obtain shows a structure with three bumps: one near threshold, one around 4350 MeV/c^2 and another at $\sim$ 4600 MeV/c^2. We aim to check whether this structure is comparable with what

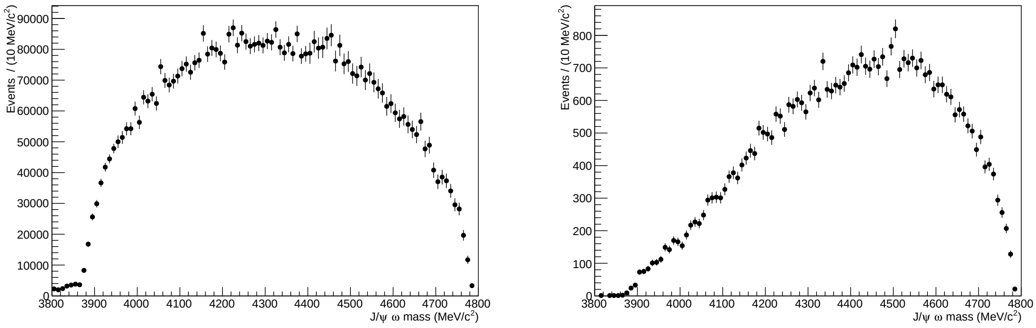

(a) The MC control sample (left) and the analysis sample after cuts 1-4 (right).

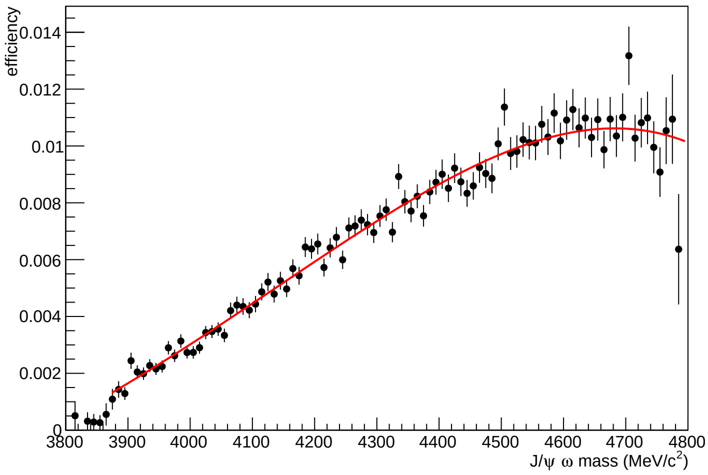

(b) Selection efficiency limited to the analysis steps 1-4.

Figure 3.26: MC distributions and efficiency for steps 1-4.

BaBar found.
Since in BaBar's article [10] efficiency-corrected data are shown and the cuts 5-7 explained in Section 3.7 are not performed, in Figure 3.27 the efficiency correction ϵ_{1-4} is applied.

A similar binning has been set in order to easily compare the two histograms: 10 MeV/c^2-wide bins are used for $M(J/\psi\ \omega) < 4000\ MeV/c^2$, while for the rest of the spectrum the bin width is increased to 50 MeV/c^2. It is evident that the shape of the mass spectrum is quite the same for the two experiments and that it cannot satisfactorily be described by a single phase-space distribution. In our case the distributions for the phase space component and the signal are not yet shown: this is added and discussed later in Chapter 4.

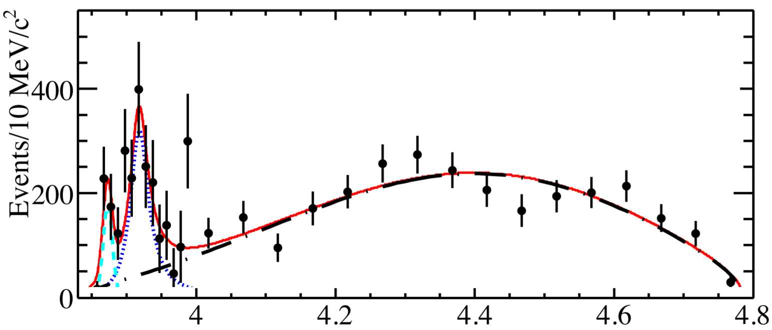

(a) BaBar's results.

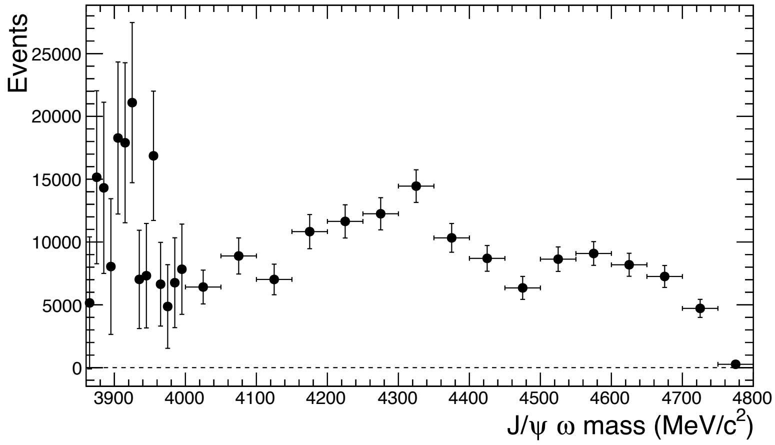

(b) Present analysis results.

Figure 3.27: Comparison with BaBar's results.

The similarity between the two spectra is encouraging as it represents a check between our analysis, which of course is not yet at a stable state and needs many improvements, and a published analysis of another experiment with completely different experimental problematics.

3.9 Analysis of $J/\psi\ \omega$ invariant mass near threshold

Consequently to the decision taken at the end of Section 3.6, the whole fit and ${}_s\mathcal{P}lot$ procedure is repeated on the sample $M(J/\psi\ \omega)\ < 4250\ MeV/c^2$. In Figure 3.28 the B mass spectrum after this cut is shown. In order to find the correct model for the signal distribution, the fit on signal MC events is repeated limiting the $J/\psi\ \omega$ mass to the same window as for data (Figure 3.29).

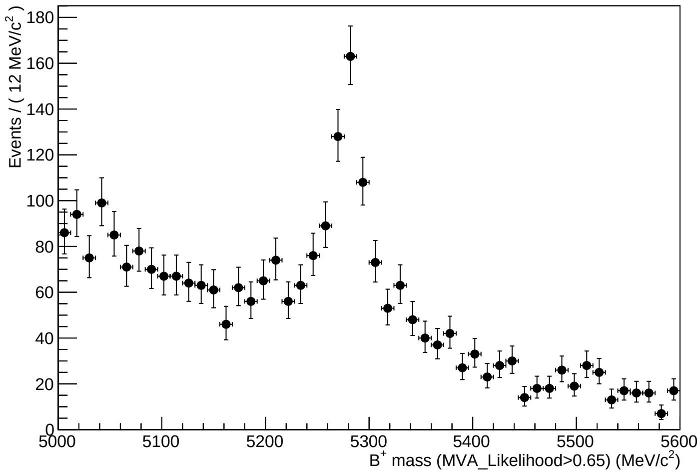

Figure 3.28: B mass distribution for $M^{setI}(J/\psi\ \omega) < 4250\ MeV/c^2$.

In this case, the most appropriate function reveals to be:

$$f_{tot} = N_{bkg} \cdot e^{\tau \cdot M} + N_{sig} \cdot (N_1 \cdot G_{narrow}(M; \mu, \sigma_{narrow}) + N_2 \cdot G_{broad}(M; \mu, \sigma_{broad})) \quad (3.9.1)$$

The broad gaussian doesn't need anymore to be bifurcated in order to fit correctly, because the peak is now much more symmetric.

Figure 3.30 shows the result of the fit on data. The number of events has considerably decreased after the cut: this implies large statistical errors on data points. In order to stabilize the fit, the standard deviations of the two gaussians are bounded as follows:

$$\begin{aligned} &\sigma_{narrow} \in [\sigma^{MC}_{narrow} - 2 \cdot \Delta\sigma^{MC}_{narrow}, \sigma^{MC}_{narrow} + 2 \cdot \Delta\sigma^{MC}_{narrow}]; \\ &\sigma_{broad} \in [\sigma^{MC}_{broad} - 2 \cdot \Delta\sigma^{MC}_{broad}, \sigma^{MC}_{broad} + 2 \cdot \Delta\sigma^{MC}_{broad}] \end{aligned} \quad (3.9.2)$$

where σ^{MC}_{narrow} and σ^{MC}_{broad} are the standard deviations obtained from the fit on MC, and $\Delta\sigma^{MC}_{narrow}$ and $\Delta\sigma^{MC}_{broad}$ are their errors.

The π^0 and ω background-subtracted mass distributions obtained with this fit are shown in Figure 3.31. For π^0 the fit with two gaussians is shown in order to compare the broad component with Figure 3.19.

The $J/\psi\ \omega$ mass distributions (Figure 3.32) from data and MC of set III are in better agreement, except for the low mass region, which is right where the excesses due to $X(3872)$ and $\chi_{c0}(2P)$ are expected to be found. A bin width compatible with the mass resolution has been used in this case. The drop on the right of the histogram is due to

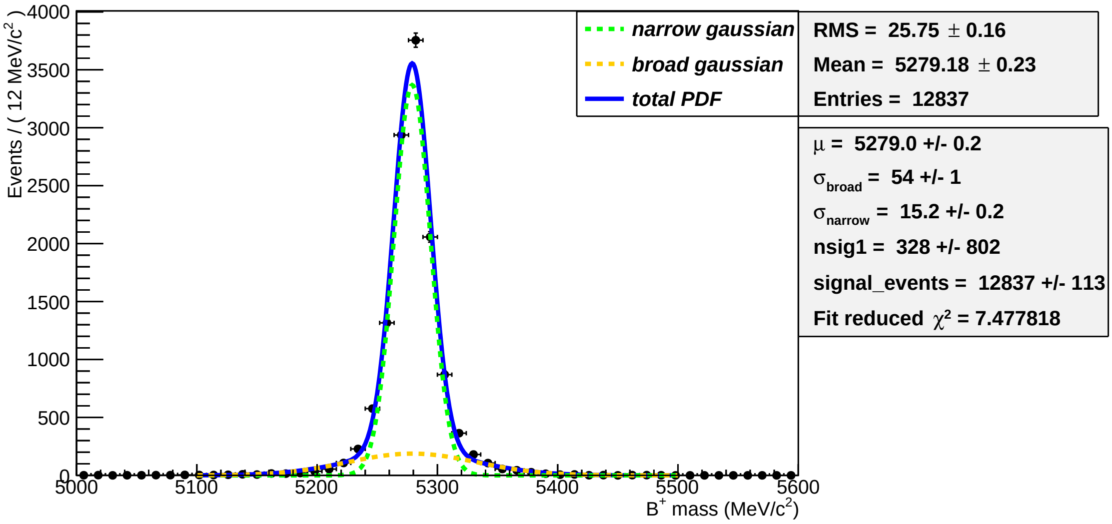

Figure 3.29: Gaussian fit on MC signal distribution.

the migration of events from one bin to another with respect to the variable in set I, on which the cut at 4250 MeV/c^2 has been applied.

The efficiency-corrected $J/\psi\ \omega$ mass distribution is shown in Figure 3.33. As new cuts 5-7 have been performed (cf. Section 3.7), here the whole efficiency ϵ_{1-7} has been used. The mass range in this plot is limited to 3860 $MeV/c^2 < J/\psi\ \omega < 4160\ MeV/c^2$: not having computed the efficiency outside this range, in fact, the drop observed for high masses and the very low mass events must be excluded from the plot.

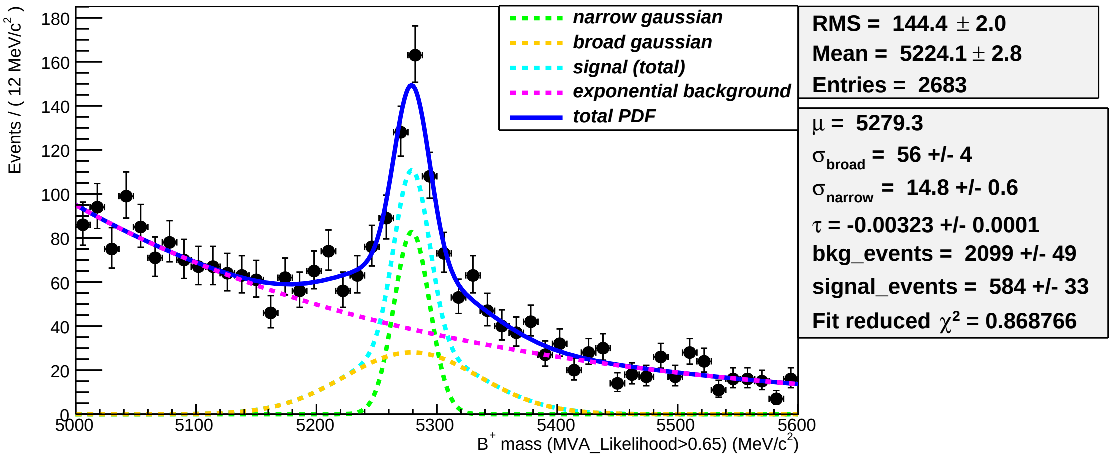

Figure 3.30: Fit on B mass distribution on data.

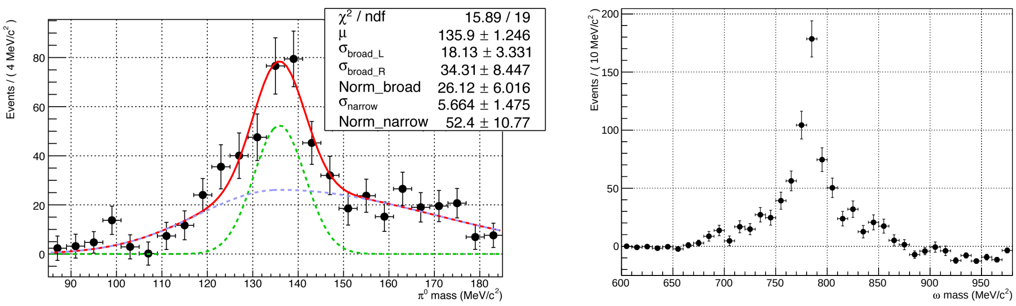

(a) π^0 (b) ω (set III)

Figure 3.31: Background-subtracted distributions of π^0 and ω masses.

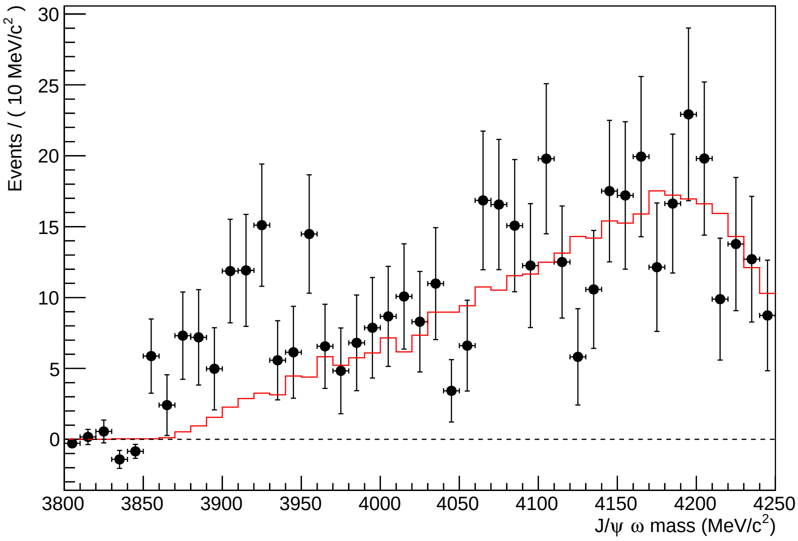

Figure 3.32: $J/\psi\,\omega$ invariant mass distribution on data (dots) and MC (red line).

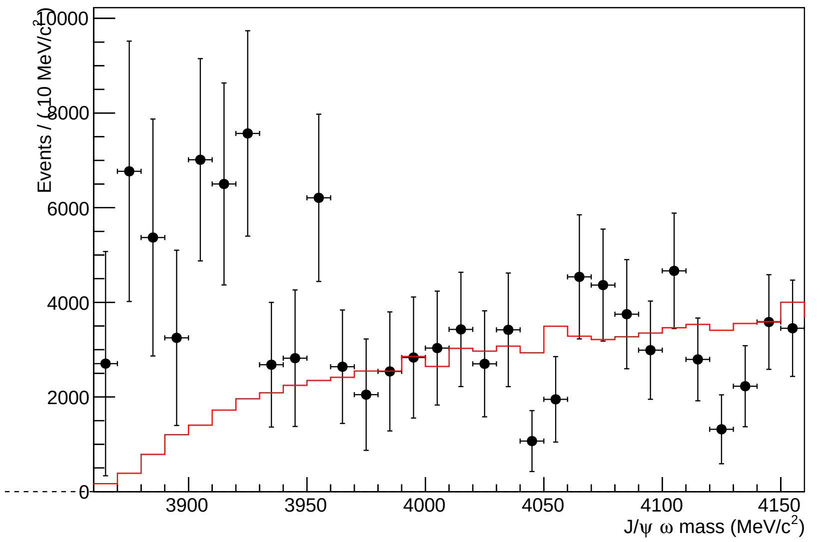

Figure 3.33: Efficiency-corrected $J/\psi\,\omega$ invariant mass spectrum for signal (dots) and MC (red line).

Chapter 4

Results

In order to estimate the number of X(3872) and $\chi_{c0}(2P)$ events, the efficiency corrected data shown in Figure 3.33 are fitted with the following distribution:

$$\begin{aligned} \mathcal{F} \; &= N_{bkg} \cdot f_{MC}(M) \;+\; N_{X(3872)} \cdot G_{X(3872)}(M; \mu_{X(3872)}, \sigma_{X(3872)}) \;+ \\ &+\; N_{\chi_{c0}(2P)} \cdot G_{\chi_{c0}(2P)}(M; \mu_{\chi_{c0}(2P)}, \sigma_{\chi_{c0}(2P)}) \end{aligned} \tag{4.0.1}$$

where M is the mass variable and:

- f_{MC} is a PDF made by interpolating at first order the MC $J/\psi\,\omega$ invariant mass distribution, meant to account for the phase-space background;
- $G_{X(3872)}$ is a gaussian distribution meant to fit the X(3872) signal with mean $\mu_{X(3872)}$ and standard deviation $\sigma_{X(3872)}$;
- $G_{\chi_{c0}(2P)}$ is a second gaussian distribution meant to fit the $\chi_{c0}(2P)$ signal with mean $\mu_{\chi_{c0}(2P)}$ and standard deviation $\sigma_{\chi_{c0}(2P)}$;
- N_{bkg} is the background yield;
- $N_{X(3872)}$ is the yield of X(3872) events;
- $N_{\chi_{c0}(2P)}$ is the yield of $\chi_{c0}(2P)$ events.

$\sigma_{X(3872)}$ has been constrained to the resolution obtained from the fit shown and discussed in Section 3.4.2 (see Figure 3.12), in correspondence to its nominal mass, while, for $\sigma_{\chi_{c0}(2P)}$, the non-negligible particle intrinsic width, $\Gamma_{\chi_{c0}(2P)} = 20 \pm 5 MeV/c^2$, is taken approximately into account, constraining this standard deviation to:

$$\sigma_{\chi_{c0}(2P)} = \sqrt{\left(\frac{\Gamma_{\chi_{c0}(2P)}}{2}\right)^2 + \delta^2_{\chi_{c0}(2P)}} \tag{4.0.2}$$

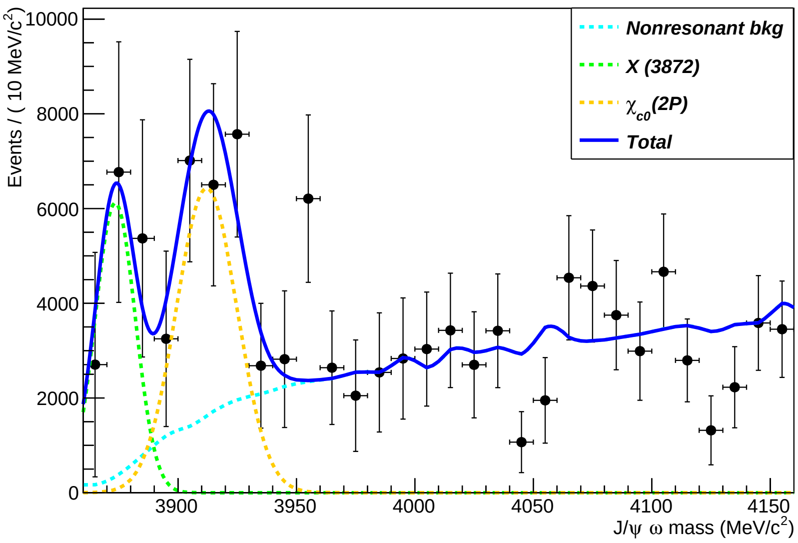

Figure 4.1: Fitted $J/\psi\ \omega$ efficiency-corrected invariant mass distribution.

Parameter	Value	Error	Unit
N_{bkg}	110130	9517	
$N_{X(3872)}$	12876	4180	
$N_{\chi_{c0}(2P)}$	20328	4549	
$\mu_{X(3872)}$	3874	4	MeV/c^2
$\sigma_{X(3872)}$	8.45	(fixed)	MeV/c^2
$\mu_{\chi_{c0}(2P)}$	3913	29	MeV/c^2
$\sigma_{\chi_{c0}(2P)}$	12.8	(fixed)	MeV/c^2
Fit χ^2/N_{dof}	0.927		

Table 4.1: Results of the fit on $J/\psi\ \omega$ invariant mass spectrum, as obtained from ROOT.

where $\delta_{\chi_{c0}(2P)}$ is the mass resolution obtained for the above-mentioned fit.

The means of the two gaussians, on the other hand, have been only bounded in the range $[3860, 3950]\ MeV/c^2$, where the corresponding signals are expected.
The result is shown in Figure 4.1, details are given in Table 4.1. As above mentioned, only the range in which the efficiency has been fitted is taken into account.

From these results the ratio between the number of $X(3872)$ and $\chi_{c0}(2P)$ can be calculated:

$$\frac{N_{X(3872)}}{N_{\chi_{c0}(2P)}} = 0.6 \pm 0.3 \tag{4.0.3}$$

While, from the measurements by BaBar:

$$\frac{BR(B^+ \to X(3872)K^+) \times BR(X(3872) \to J/\psi\,\omega)}{BR(B^+ \to \chi_{c0}(2P)K^+) \times BR(\chi_{c0}(2P) \to J/\psi\,\omega)} = 0.2 \pm 0.1 \qquad (4.0.4)$$

The errors in (4.0.3) are only statistical. The analysis of the systematic effects which can affect this measurement lies outside the objectives of this thesis. In particular, the efficiency calculation near threshold is quite critical and can affect this result in a very significant way. The new MC simulation with the enrichment in statistics in the low mass region can help in improving this measurement.

Conclusions

In conclusion, the analysis presented in this thesis led to the observation of two excesses in the $J/\psi\,\omega$ invariant mass distribution in the decay $B^+ \to J/\psi\,\omega\,K$ corresponding to the masses of the $\chi_{c0}(2P)$ meson and the exotic particle $X(3872)$. The results are found to be comparable with BaBar's.
An estimation of the ratio between the branching fraction of the two particles' production for this decay gives 0.6 ± 0.3, while BaBar obtained 0.2 ± 0.1. The difference between the two results is 0.4 ± 0.3, consistent with zero within less than 2 standard deviations.

This analysis is open to further developments: the low statistics of the Monte Carlo sample in the mass threshold range will be enriched with a new MC production which is currently under development, to improve the efficiency correction. An inclusive MC sample - containing all the decays of the type $B \to J/\psi + m$, where m can indicate one or more particles - is going to be analyzed, allowing to upgrade the B mass fit model identifying possible sources of background not yet considered. Furthermore, the source of the unidentified structure in the $J/\psi\,\omega$ spectrum around 4300 MeV must be studied.

Last but not least, the Run II of LHCb from year 2015 to 2018 will considerably increase the available statistic of real data, hopefully allowing precise measurements of the BR. An angular analysis may also be achievable, in order to study the X(3872) quantum numbers, which could provide important information about its exotic nature.

APPENDICES

Appendix A

The ${}_s\mathcal{P}lot$ technique

The ${}_s\mathcal{P}lot$ technique is an analysis method which applies to a data sample consisting of several sources of events merged together (e.g. a source of signal and one of background).

The set of variables describing these events is assumed to be made of two subsets. The first subset, which we will refer to as a (unique) *discriminating* variable, y, consists of variables for which the distributions of all the sources of events are known. For the second subset, on the other hand, the distributions of some sources of events are either truly unknown or considered as such; here below, these variables are collectively referred to as a (unique) *control* variable, x.

The aim of this technique is to reconstruct the distributions for the control variable's sources indipendently, without making use of any *a priori* knowledge on this variable. For the ${}_s\mathcal{P}lot$ technique to be valid, the control variable must be uncorrelated with the discriminating variable.

A.0.1 The method

Consider an unbinned extended maximum Likelihood analysis of a data sample such as the one described above. The (unbinned) log-Likelihood is expressed as:

$$\mathcal{L} = \sum_{e=1}^{N} \ln \left\{ \sum_{i=1}^{N_s} N_i f_i(y_e) \right\} - \sum_{i=1}^{N_s} N_i \tag{A.0.1}$$

where

- N is the total number of events considered;

- N_s is the number of species of events populating the data sample (i.e. the different sources of events, e.g. signal and background)
- N_i is the number of events of the i^{th} species;
- y represents the set of discriminating variables, which can be correlated with each other;
- $f_i(y_e|\vec{r}_S)$ is the e^{th} event value of the analytic PDF f_i describing the y distribution for the i^{th} species, $\vec{r}_S$ being the vector of its fitting parameters.

The yields N_i and the parameters $\vec{r}_i$ are determined by maximizing the above log-Likelihood.
Once these values are extracted from the fit, and thus the PDFs of all the species are fully determined for the discriminating variables, the $_s\mathcal{P}lot$ purpose is to use these PDFs for assigning to each event a set of weights (thereafter called *sWeights*), one for each species.
This is done with the aim of being able to build, for the control variables, separate histograms for the different species, thus unfolding the overall distribution from the mixed sample into the sub-distributions of the various species.

A first, naive, guess of how the sWeights should be calculated, could be

$$\mathcal{P}_n(y_e) \doteq \frac{N_n f_n(y_e)}{\sum_{k=1}^{N_s} N_k f_k(y_e)} \tag{A.0.2}$$

but this only applies, as it will be clear hereinafter, when the variable x is totally correlated with y, namely x is a function of y.
Using these weights we could build an estimate, $\tilde{M}_n$, of the x-distribution of the n^{th} species:

$$N_n \tilde{M}_n(\overline{x})\delta x \equiv \sum_{e\subset\delta x} \mathcal{P}_n(y_e) \tag{A.0.3}$$

where the sum runs over all the events for which x_e is between $\overline{x} - \delta x/2$ and $\overline{x} + \delta x/2$.
This procedure provides an estimate of the true distribution $M_n(x)$. This can be shown as follows.
The sum in Eq. (A.0.3) can be replaced, on the average, by the integral

$$\left\langle \sum_{e\subset\delta x} \right\rangle \to \int dy \sum_{j=1}^{N_S} N_j f_j \delta(x(y) - \overline{x})\delta x \tag{A.0.4}$$

thus obtaining

$$\begin{aligned}\left\langle N_n\tilde{M}_n(\overline{x})\right\rangle &= \int dy \sum_{j=1}^{N_S} N_j f_j(y)\delta(x(y)-\overline{x})\mathcal{P}_n(y) = \\ &= \int dy \sum_{j=1}^{N_S} N_j f_j(y)\delta(x(y)-\overline{x})\frac{N_n f_n(y)}{\sum_{j=1}^{N_s} N_k f_k(y)} = \\ &= N_n \int dy\delta(x(y)-\overline{x})f_n(y) \equiv \\ &\equiv N_n M_n(\overline{x})\end{aligned} \tag{A.0.5}$$

Plots obtained using weights in Eq. (A.0.2) are referred to as $_{in}\mathcal{P}lots$: as above mentioned, they provide a correct means to reconstruct Mn(x) only insofar as the variable considered is in the set of discriminating variables y.
This kind of plot is, nevertheless, faulty in some cases, because the PDFs of x enter implicitly in the weights definition. [51]

Moving to the interesting case, in which x and y are not correlated, Eq. (A.0.5) does not hold any more; in fact, the PDF of x should now enter in Eq. (A.0.4), making the last equality in Eq. (A.0.5) false. Indeed, in this case

$$\begin{aligned}\left\langle N_n\tilde{M}_n(\overline{x})\right\rangle &= \int\int dydx \sum_{j=1}^{N_S} N_j M_j(x) f_j(y)\delta(x(y)-\overline{x})\mathcal{P}_n(y) = \\ &= \int dy \sum_{j=1}^{N_S} N_j M_j(\overline{x}) f_j(y)\frac{N_n f_n(y)}{\sum_{j=1}^{N_S} N_k f_k(y)} = \\ &= N_n \sum_{j=1}^{N_S} M_j(\overline{x})\left[N_j \int dy \frac{f_n(y) f_j(y)}{\sum_{k=1}^{N_S} N_k f_k(y)}\right] \neq \\ &\neq N_n M_n(\overline{x}).\end{aligned} \tag{A.0.6}$$

The reason is that the *correction term* in square brackets is not identical to the kronecker symbol δ_{jn}.
The $_{in}\mathcal{P}lots$ distribution $N_n\tilde{M}_n$ obtained using the naive weight is a linear combination of the true distributions M_j.
If the y variable was totally discriminating the equality would hold again. In fact, in that case $f_{j\neq n}(y)$ would vanish if $f_n(y)$ is non zero (that is nothing more that an other way of saying that y is totally discriminating). Thus, the term in square brackets would become

$$N_j\delta_{jn} \int dy \frac{f_n^2(y)}{N_n f_n(y)} = \delta_{jn}. \tag{A.0.7}$$

Anyway this case is purely academic, because if y were totally discriminating, plotting the distribution of x for the n^{th} species would be possible simply applying cuts on y, thus obtaining a pure sample.

Coming back to the generale case, the correction term is on closer inspection related to the inverse of the covariant matrix element

$$\mathbf{V}_{nj}^{-1} = \frac{\partial^2(-\mathcal{L})}{\partial N_n \partial N_j} = \sum_{e=1}^{N} \frac{f_n(y_e) f_j(y_e)}{\left(\sum_{k=1}^{N_S} N_k f_k(y_e)\right)^2}. \tag{A.0.8}$$

Replacing the sum by an integral as in Eq. (A.0.4), the variance matrix can be expressed as

$$\begin{aligned} \left\langle \mathbf{V}_{nj}^{-1} \right\rangle &= \int\int dy dx \sum_{l=1}^{N_s} N_l M_l(x) f_l(y) \frac{f_n(y) f_j(y)}{(\sum_{k=1}^{N_S} N_k f_k(y))^2} = \\ &= \int dy \sum_{l=1}^{N_s} N_l f_l(y) \frac{f_n(y) f_j(y)}{(\sum_{k=1}^{N_S} N_k f_k(y))^2} \int dx M_l(x) = \\ &= \int dy \frac{f_n(y) f_j(y)}{\sum_{k=1}^{N_S} N_k f_k(y)}. \end{aligned} \tag{A.0.9}$$

Using this result in Eq. (A.0.6) and inverting the equation, one obtains

$$N_n M_n(\overline{x}) = \sum_{j=1}^{N_S} \langle \mathbf{V}_{nj} \rangle \left\langle \tilde{M}_j(\overline{x}) \right\rangle \tag{A.0.10}$$

In other words, the correct *sWeights* to be used in Eq. (A.0.3) are now

$${}_s\mathcal{P}_n(y_e) = \frac{\sum_{j=1}^{N_s} \mathbf{V}_{nj} f_j(y_e)}{\sum_{k=1}^{N_s} N_k f_k(y_e)} \tag{A.0.11}$$

and thus the distribution of the control variable x for the n^{th} species can be obtained by building the following histogram:

$$N_{ns} \tilde{M}_n(\overline{x}) \delta x \equiv \sum_{e \subset \delta x} {}_s\mathcal{P}_n(y_e). \tag{A.0.12}$$

The case in which x and y are partially correlated, as well as other $_s\mathcal{P}lot$ properties [51] are not illustrated here for the sake of conciseness.

Coming finally to the statistical uncertainties, they can be defined in each bin as

$$\sigma\left[N_{n\,s}\tilde{M}_n(x)\delta(x)\right] = \sqrt{\sum_{e\subset\delta x}({}_s\mathcal{P}_n)^2}. \tag{A.0.13}$$

In fact

$$\begin{aligned}
&\left\langle\left(\sum_{e\subset\delta x}{}_s\mathcal{P}_n\right)^2\right\rangle - \left\langle\sum_{e\subset\delta x}{}_s\mathcal{P}_n\right\rangle^2 = \\
&= \langle N_{\delta x}\rangle\left\langle{}_s\mathcal{P}_n^2\right\rangle + \langle N_{\delta x}(N_{\delta x}-1)\rangle\left\langle{}_s\mathcal{P}_n\right\rangle^2 - \langle N_{\delta x}\rangle^2\left\langle{}_s\mathcal{P}_n\right\rangle^2 = \\
&= \langle N_{\delta x}\rangle\left\langle{}_s\mathcal{P}_n^2\right\rangle + \left(\left\langle N_{\delta x}^2\right\rangle - \langle N_{\delta x}\rangle\right)\left\langle{}_s\mathcal{P}_n\right\rangle^2 - \langle N_{\delta x}\rangle^2\left\langle{}_s\mathcal{P}_n\right\rangle^2 = \\
&= \langle N_{\delta x}\rangle\left\langle{}_s\mathcal{P}_n^2\right\rangle + \Big(\langle N_{\delta x}\rangle + \langle N_{\delta x}\rangle^2 - \langle N_{\delta x}\rangle\Big)\left\langle{}_s\mathcal{P}_n\right\rangle^2 - \langle N_{\delta x}\rangle^2\left\langle{}_s\mathcal{P}_n\right\rangle^2 = \\
&= \langle N_{\delta x}\rangle\left\langle{}_s\mathcal{P}_n^2\right\rangle = \left\langle\sum_{e\subset\delta x}({}_s\mathcal{P}_n)^2\right\rangle = \left\langle\sigma^2\left[N_n\;{}_s\tilde{M}_n\delta x\right]\right\rangle
\end{aligned} \tag{A.0.14}$$

Furthermore, as shown in [51], the sum in quadrature of the uncertainties in Eq. (A.0.13) reproduces the statistical uncertainty on the yield N_n, as it is provided by the fit.

Bibliography

[1] The gaudi project. `http://proj-gaudi.web.cern.ch/proj-gaudi/`.

[2] S. Agostinelli et al. GEANT4: A Simulation toolkit. *Nucl.Instrum.Meth.*, A506:250–303, 2003.

[3] Mohammad T. AlFiky, Fabrizio Gabbiani, and Alexey A. Petrov. X(3872): Hadronic molecules in effective field theory. *Phys.Lett.*, B640:238–245, 2006.

[4] V.E et al. Barnes. Observation of a Hyperon with Strangeness Minus Three. *Phys. Rev.Lett.*, 12:204, 1964.

[5] C. Bignamini, B. Grinstein, F. Piccinini, A. D. Polosa, and C. Sabelli. Is the $X(3872)$ Production Cross Section at $\sqrt{s}$=1.96 TeV Compatible with a Hadron Molecule Interpretation? *Phys. Rev. Lett.*, 103:162001, Oct 2009.

[6] R. Brun and F. Rademakers. ROOT: An object oriented data analysis framework. *Nucl.Instrum.Meth.*, A389:81–86, 1997.

[7] Frank E. Close and Philip R. Page. The D*0 anti-D0 threshold resonance. *Phys.Lett.*, B578:119–123, 2004.

[8] BABAR Collaboration. Study of the $B^- \to J/\psi K^-\pi^+\pi^-$ decay and measurement of the $B^- \to X(3872)K^-$ branching fraction. *Phys. Rev. D*, 71:071103, Apr 2005.

[9] BABAR Collaboration. Search for $B^+ \to X(3872)K^+$, $X(3872) \to J/\psi\gamma$. *Phys. Rev. D*, 74:071101, Oct 2006.

[10] BaBar Collaboration. Evidence for the decay $X(3872) \to J/\psi\omega$. *Phys.Rev.*, D82:011101, 2010.

[11] BABAR Collaboration. Study of $X(3915) \to J/\psi\omega$ in two-photon collisions. *Phys. Rev. D*, 86:072002, Oct 2012.

[12] Belle Collaboration. Observation of a narrow charmonium - like state in exclusive $B^+ \to K^+\pi^+\pi^- J/\psi$ decays. *Phys.Rev.Lett.*, 91:262001, 2003.

[13] Belle Collaboration. Evidence for $X(3872) \to \gamma J/\psi$ and the sub-threshold decay $X(3872) \to \omega J/\psi$. 2005.

[14] Belle Collaboration. Observation of a near-threshold $\omega J/\psi$ mass enhancement in exclusive $B \to K\omega J/\psi$ decays. *Phys.Rev.Lett.*, 94:182002, 2005.

[15] Belle Collaboration. Study of $B \to X(J/\psi\pi^+\pi?-)K$ decays. *Belle-CONF-0711*, 2007.

[16] Belle Collaboration. Observation of a Resonancelike Structure in the $\pi^{+-}\psi'$ Mass Distribution in Exclusive $B \to K\pi^{+-}\psi'$ Decays. *Phys. Rev. Lett.*, 100:142001, Apr 2008.

[17] Belle Collaboration. Observation of two resonancelike structures in the $\pi^+\chi_{c1}$ mass distribution in exclusive $\overline{B}^0 \to K^-\pi^+\chi_{c1}$ decays. *Phys. Rev. D*, 78:072004, Oct 2008.

[18] CDF Collaboration. Observation of the narrow state $X(3872)$ $rightarrow J/\psi\pi^+\pi^-$ in $p\overline{p}$ collisions at $\sqrt{s} = 1.96$ TeV. *Phys.Rev.Lett.*, 93:072001, 2004.

[19] CDF Collaboration. Measurement of the Dipion Mass Spectrum in $X(3872) \to J/\psi\pi^+\pi^-$ Decays. *Phys. Rev. Lett.*, 96:102002, Mar 2006.

[20] CDF Collaboration. Analysis of the quantum numbers J^{PC} of the $X(3872)$. *Phys.Rev.Lett.*, 98:132002, 2007.

[21] D0 Collaboration. Observation and properties of the X(3872) decaying to $J/\psi\pi^+\pi^-$ in $p\overline{p}$ collisions at $\sqrt{s} = 1.96$ TeV. *Phys.Rev.Lett.*, 93:162002, 2004.

[22] LHCb Collaboration. The evtgen project. `http://lhcb-release-area.web.cern.ch/LHCb-release-area/DOC/gauss/`.

[23] LHCb Collaboration. LHCb calorimeters: Technical Design Report. 2000.

[24] LHCb Collaboration. LHCb magnet: Technical Design Report. 2000.

[25] LHCb Collaboration. LHCb RICH: Technical Design Report. 2000.

[26] LHCb Collaboration. LHCb VELO (VErtex LOcator): Technical Design Report. 2001.

[27] LHCb Collaboration. LHCb muon system: Technical Design Report. 2001.

[28] LHCb Collaboration. LHCb outer tracker: Technical Design Report. 2001.

[29] LHCb Collaboration. LHCb online system, data acquisition and experiment control: Technical Design Report. 2001.

[30] LHCb Collaboration. LHCb inner tracker: Technical Design Report. 2002. revised version number 1 submitted on 2002-11-13 14:14:34.

[31] LHCb Collaboration. LHCb trigger system: Technical Design Report. 2003. revised version number 1 submitted on 2003-09-24 12:12:22.

[32] LHCb Collaboration. LHCb computing: Technical Design Report. 2005. Submitted on 11 May 2005.

[33] LHCb Collaboration. The LHCb Detector at the LHC. *JINST*, 3:S08005, 2008.

[34] LHCb Collaboration. Determination of the X(3872) meson quantum numbers. *Phys.Rev.Lett.*, 110:222001, 2013.

[35] The BESIII collaboration. Observation of a Charged Charmoniumlike Structure in $e^+e^- \to \pi^+\pi^- J/\psi$ at $\sqrt{s} = 4.26$ GeV. *Phys.Rev.Lett.*, 110:252001, 2013.

[36] J. F. Cornwell. *Group Theory in Physiscs*. Academic Press, 1997.

[37] N Drenska, R. Faccini, F. Piccinini, A. Polosa, F. Renga, and C. Sabelli. New Hadronic Spectroscopy. *Riv. Nuovo Cim.*, 033:633–712, 2010.

[38] G. Fraser. *The Particle Century*. Taylor and Francis / Institute of Physics Publishing, 1st ed. edition, 1998.

[39] M. Gell-Mann. A schematic model of baryons and mesons. *Phys. Rev. Lett.*, 8:214–2, 1964.

[40] Paola Gianotti. Results and perspectives in hadron spectroscopy. *Physica Scripta*, 2012(T150):014014, 2012.

[41] S. Godfrey and S. L. Olsen. The Exotic XYZ Charmonium-like Mesons. *Ann.Rev.Nucl.Part.Sci.*, 58:51–73, 2008.

[42] Q. Ho-Kim and Xuan-Yem Pham. *Elementary Particles and Their Interactions: Concepts and Phenomena*. Springer-Verlag, 1998.

[43] Andreas Hocker, J. Stelzer, F. Tegenfeldt, H. Voss, K. Voss, et al. TMVA - Toolkit for Multivariate Data Analysis. *PoS*, ACAT:040, 2007.

[44] L. D. Landau, E. M. Liftshitz, and L. P. Pitaevskii. *Electrodynamic of Continuous Media*. Pergamon Press, New York, 2nd ed. edition, 1984.

[45] L. Maiani, F. Piccinini, A.D. Polosa, and V. Riquer. Diquark-antidiquarks with hidden or open charm and the nature of X(3872). *Phys.Rev.*, D71:014028, 2005.

[46] C. A. Meyer and Y. Van Haarlem. The Status of Exotic-quantum-number Mesons. *Phys.Rev.*, C82:025208, 2010.

[47] M Needham. Clone Track Identification using the Kullback-Liebler Distance. Technical Report LHCb-2008-002. CERN-LHCb-2008-002. LPHE-2008-002, CERN, Geneva, Jan 2008.

[48] M Needham. Performance of the LHCb Track Reconstruction Software. Technical Report LHCb-2007-144. CERN-LHCb-2007-144, CERN, Geneva, Jan 2008.

[49] Y. Ne'enam. A schematic model of baryons and mesons. *Phys. Lett.*, 26:222, 1961.

[50] J. Neyman and E. S. Pearson. On the problem of the most efficient tests of statistical hypotheses. *Philosophical Transactions of the Royal Society of London. Series A, Containing Papers of a Mathematical or Physical Character*, 231:289–337, 1933.

[51] M. Pivka and F.R. Le Diberder. sPlot: a statistical tool to unfold data distributions. *arXiv:physics/0402083v3*, 2005.

[52] Torbjörn Sjöstrand, Stephen Mrenna, and Peter Skands. PYTHIA 6.4 physics and manual. *Journal of High Energy Physics*, 2006(05):026, 2006.

[53] J. Smit. *Introduction to Quantum Fields on a Lattice*. Cambridge University Press, 2002.

[54] Fl. Stancu. *Group Theory in Subnuclear Physics*. Oxford University Press, 1st ed. edition, 1997.

[55] Warwick Development Team. The gauss project. `http://evtgen.warwick.ac.uk`.

[56] Wu-Ki Tung. *Group Theory in Physiscs*. World Scientific, Singapore, 1985.

[57] W Verkerke and D Kirkby. The RooFit toolkit for data modeling. Technical Report arXiv:physics/0306116 [physics.data-an], 2003.

[58] G. Zweig. An SU(3) model for strong interaction symmetry and its breaking. Version 1. 1964.